Targeted degradation of oncogenic KRAS^{G12V} triggers antitumor immunity in lung cancer models

Dezhi Li[1,19,#], Ke Geng[1,#], Yuan Hao[2,#], Jiajia Gu[3,#], Saurav Kumar[4,#], Annabel T. Olson[4], Christina C. Kuismi[4], Hye Mi Kim[3,5], Yuanwang Pan[1], Fiona Sherman[1], Asia M. Williams[3,5], Yiting Li[3,6], Fei Li[7,8], Ting Chen[1], Cassandra Thakurdin[1], Michela Ranieri[1], Mary Meynardie[1], Daniel S. Levin[1], Janaye Stephens[1], Alison Chafitz[1], Joy Chen[4], Mia S. Donald-Paladino[4], Jaylen M. Powell[1], Ze-Yan Zhang[9], ,Wei Chen[10], Magdalena Ploszaj[1], Han Han[1], Shengqing Stan Gu[11], Tinghu Zhang[12], Baoli Hu[3,13], Benjamin A. Nacev[3,14,15], Medard Ernest Kaiza[3,5], Alice H. Berger[4], Xuerui Wang[3,5], Jing Li[3,5], Xuejiao Sun[3], Yang Liu[16], Xiaoyang Zhang[17], Tullia C. Bruno[3,5], Nathanael S. Gray[12], Behnam Nabet[4,18*], Kwok-Kin Wong[1*], Hua Zhang[3,14*]

[1]Division of Hematology and Medical Oncology, Laura and Isaac Perlmutter Cancer Center, New York University Langone Health, New York, NY 10016, USA

[2]Applied Bioinformatics Laboratories, Office of Science and Research, New York University Grossman School of Medicine, New York, NY 10016, USA

[3]Hillman Cancer Center, UPMC, Pittsburgh, PA 15232 USA

[4]Human Biology Division, Fred Hutchinson Cancer Center, Seattle, WA 98109, USA

[5]Department of Immunology, University of Pittsburgh, Pittsburgh, PA 15261, USA

[6]School of Medicine, Tsinghua University, Beijing, China

[7]Department of Pathology, School of Basic Medical Sciences, Fudan University, Shanghai, China

[8]Frontier Innovation Center, School of Basic Medical Sciences, Fudan University, Shanghai, China

[9]Department of Radiation Oncology, New York University Grossman School of Medicine, New York, NY 10016, USA

[10]Division of Pulmonary Medicine, Department of Pediatrics, UPMC Children's Hospital of Pittsburgh and University of Pittsburgh, Pittsburgh, PA, USA

[11]Department of Hematopoietic Biology and Malignancy, University of Texas MD Anderson Cancer Center, Houston, TX, USA

[12]Department of Chemical and Systems Biology, Chem-H and Stanford Cancer Institute, Stanford School of Medicine, Stanford University, Stanford, CA 94305, USA

[13]Department of Neurological Surgery, University of Pittsburgh School of Medicine, Pittsburgh, PA 15261, USA

[14]Department of Medicine, Division of Hematology/Oncology, University of Pittsburgh School of Medicine, Pittsburgh, PA 15261, USA

[15]Department of Pathology, University of Pittsburgh School of Medicine, Pittsburgh, PA 15261, USA

[16]Department of Bioengineering, University of Illinois Urbana-Champaign, Urbana, IL 61801, USA

[17]Department of Oncological Sciences, Huntsman Cancer Institute, University of Utah, Salt Lake City, UT 84112, USA

[18]Department of Pharmacology, University of Washington, Seattle, WA 98195, USA

[19]Present address: Department of Pulmonary and Critical Care Medicine, Shandong Provincial Hospital Affiliated to Shandong First Medical University, Jinan, 250021, China

Keywords. KRAS, degradation, mouse modeling, antitumor immunity, lung cancer

[#]DL, KG, YH, JG, and SK contributed equally to this article.

[*]**Corresponding Authors**: Hua Zhang, Hillman Cancer Center, UPMC, Department of Medicine, Division of Hematology/Oncology, University of Pittsburgh School of Medicine, 5117 Centre Avenue, Pittsburgh, PA 15261. Phone: 412-864-7742; Email: huz59@pitt.edu

Kwok-Kin Wong, Laura and Isaac Perlmutter Cancer Center, New York University Langone Medical Center, 550 First Avenue, New York, NY 10016, USA. Phone: 212-263-9203; Email: Kwok-Kin.Wong@nyulangone.org

Behnam Nabet, Human Biology Division, Fred Hutchinson Cancer Center, 1100 Fairview Avenue N., Seattle, WA 98109, USA. Phone: 206-667-4052; Email: bnabet@fredhutch.org

Conflict-of-interest statement

TZ is a scientific founder, equity holder, and consultant of Matchpoint, and equity holder of Shenandoah. NSG is a Scientific Founder, member of the SAB, and equity holder in C4 Therapeutics, Syros, Soltego (board member), B2S/Voronoi, Allorion, Lighthorse, Cobroventures, GSK, Larkspur (board member), Shenandoah (board member), and Matchpoint. The Gray lab receives research funding from Springworks and Interline. BN and NSG are inventors on a patent application related to the dTAG system (WO/2020/146250). BN is an inventor on patent applications related to the dTAG system (WO/2017/024318, WO/2017/024319, WO/2018/148440, and WO/2018/148443). The Nabet laboratory receives or has received research funding from Mitsubishi Tanabe Pharma America, Inc. KKW is a founder and equity holder of G1 Therapeutics and has sponsored research agreements with MedImmune, Takeda, TargImmune, Bristol-Myers Squibb, Mirati, Merus, and Alkermes, and consulting and sponsored research agreements with AstraZeneca, Janssen, Pfizer, Novartis, Merck, Ono, and Array. No disclosures were reported by the other authors.

Abstract

KRAS is the most frequently mutated oncogene in lung adenocarcinoma, with *G12C* and *G12V* being the most predominant forms. Recent breakthroughs in $KRAS^{G12C}$ inhibitors have transformed the clinical management of patients with *G12C* mutation and advanced our understanding of its function. However, little is known about the targeted disruption of $KRAS^{G12V}$, partly due to a lack of specific inhibitors. Here, we leverage the degradation tag (dTAG) system to develop a $KRAS^{G12V}$ transgenic mouse model. We explore the therapeutic potential of $KRAS^{G12V}$ degradation and characterize its impact on the tumor microenvironment (TME). Our study reveals that degrading $KRAS^{G12V}$ abolishes lung and pancreatic tumors in mice and causes a robust inhibition of KRAS-regulated cancer intrinsic signaling. Importantly, targeted degradation of $KRAS^{G12V}$ reprograms the TME towards a stimulatory milieu and drives antitumor immunity, elicited mainly by effector and cytotoxic $CD8^+$ T cells. Our work provides important insights into the impact of degrading $KRAS^{G12V}$ on both tumor progression and immune response, highlighting degraders as a powerful strategy for targeting *KRAS* mutant cancers.

Introduction

Non-small cell lung cancer (NSCLC) is one of the leading causes of cancer death worldwide (1). *KRAS* is the most frequently mutated oncogene in lung adenocarcinoma, the most common subtype of NSCLC (2). Approximately 30% of patients with lung adenocarcinoma harbor *KRAS* mutations, which are most commonly *G12C* and *G12V* (3). Directly targeting KRAS has been historically difficult until the recent development of $KRAS^{G12C}$-specific inhibitors including ARS-1620, AMG-510, and MRTX849 (4-7). These inhibitors have shown strong antitumor effects in $KRAS^{G12C}$-mutated lung adenocarcinoma preclinical models and patients (6, 8, 9). Notably, based on the positive clinical benefit observed in large clinical trials, the Food and Drug Administration (FDA) recently approved AMG-510 (Sotorasib) for the treatment of patients with $KRAS^{G12C}$-mutated NSCLC. Despite this remarkable breakthrough, Sotorasib demonstrates an approximately 30% response rate in patients with lung cancer (9, 10), with the rapid emergence of drug resistance (11-13). Furthermore, in stark contrast to the substantial advances in $KRAS^{G12C}$ drug discovery, there are currently no approved specific inhibitors for $KRAS^{G12V}$. As drug discovery efforts focus on $KRAS^{G12V}$, an improved understanding of the biological consequences of $KRAS^{G12V}$ disruption on tumor intrinsic signaling and the tumor microenvironment (TME) *in vivo* is necessary.

Targeted protein degradation has emerged as a powerful therapeutic approach to target oncogenic drivers (14-17). PROteolysis TArgeting Chimeras (PROTACs) are a class of small molecule degraders that bind a target protein and E3 ligase, leading to target protein ubiquitination and rapid proteasome-mediated degradation (18). PROTACs are advantageous over inhibitors due to their ability to abolish all protein activity including scaffolding functions (19, 20). We and others have endeavored to develop PROTACs to degrade $KRAS^{G12C}$, which has proven to be challenging (21, 22). While PROTACs such as LC-2 are capable of degrading $KRAS^{G12C}$, the benefits and liabilities of KRAS degradation *in vivo* remain unclear (22). Furthermore, although pan-KRAS degraders are in preclinical development (23-25) and $KRAS^{G12D}$ degraders are in clinical trials (NCT05382559) (26), the consequences of targeted $KRAS^{G12V}$ degradation in immune-competent models and the characterization of $KRAS^{G12V}$-selective degraders remain largely unexplored. Prior to the investment in the development of degraders, strategies to model the pharmacological degradation of drug targets are necessary.

As a solution to this challenge, we developed a versatile approach known as the degradation tag (dTAG) system to deplete tagged proteins *in vitro* and *in vivo* (27, 28). In this approach, a protein is expressed with an $FKBP12^{F36V}$-tag and is targeted for degradation using dTAG molecules that recruit an E3 ubiquitin ligase. We previously demonstrated that the dTAG system can be effectively employed to study the consequences of rapid and selective $KRAS^{G12V}$ degradation in several cellular models (27-29). We and others have extensively applied the dTAG system to degrade diverse targets including oncoproteins, transcription factors, chromatin regulators, and kinases, illustrating the utility of the dTAG system for drug target validation and discovery (27, 28, 30, 31).

Mouse models are invaluable for understanding the biology of lung cancer, identifying potential therapeutic targets, and testing new treatments in a preclinical setting. Previous studies utilizing $KRAS^{G12V}$ mouse models have advanced our understanding of $KRAS^{G12V}$-driven lung cancer and nominated new potential therapeutic approaches (32-35). In this study, to develop a platform for target drug validation *in vivo*, we advanced the dTAG system to establish a genetically engineered mouse model (GEMM) harboring $KRAS^{G12V}$ amendable for specific and rapid degradation. This powerful model enabled us to comprehensively characterize the therapeutic potential of degrading $KRAS^{G12V}$. Utilizing this $KRAS^{G12V}$ GEMM, we were able to dissect the tumor intrinsic responses as well as extrinsic effects including the impact on the TME upon degrading $KRAS^{G12V}$.

Our findings offer strong evidence for the promise of developing degraders targeting mutant KRAS in cancer and also establish an *in vivo* platform for drug target discovery and validation.

Results

Establishing a GEMM for targeted degradation of KRAS^{G12V} in lung cancer.

Chemical-genetic degron strategies for achieving rapid, selective, and robust target protein loss have emerged as powerful approaches for biological study and drug target validation (31, 36). However, there are limited generalizable targeted degradation strategies available to study drug target loss *in vivo*. KRAS^{G12V} is an ideal drug target to evaluate the consequences of targeted degradation. Critically, the impact of KRAS^{G12V} protein degradation on tumorigenesis, intrinsic signaling, and the TME is poorly understood, which is due to limited relevant mouse models and specific KRAS^{G12V} inhibitors or degraders. To address these challenges, we set out to leverage the dTAG system (27, 28) to establish a GEMM harboring *KRAS^{G12V}* amendable for specific and rapid degradation (detailed in the Methods Section). In our approach, dTAG molecules bind an FKBP12^{F36V}-tag and recruit an E3 ubiquitin ligase in proximity to induce FKBP12^{F36V}-fusion protein degradation (**Figure 1A** and **Supplemental Figure 1A**). We previously demonstrated that our dTAG molecules known as dTAG^{V}-1 and dTAG-13, which recruit von Hippel-Lindau (VHL) or cereblon (CRBN), respectively, are selective and degrade KRAS^{G12V} in several cellular models, including pancreatic ductal adenocarcinoma cell lines (27, 28). We also demonstrated that these dTAG molecules display suitable pharmacokinetic (PK) and pharmacodynamic (PD) properties to degrade tagged fusions in xenograft mouse models (27, 28, 37). Recent work has further confirmed the tolerability of dTAG molecules *in vivo* and has shown that dTAG molecules effectively degrade FKBP12^{F36V}-tagged proteins in embryonic stages of mouse development (38), in several mouse organs (39), and patient-derived xenograft models (40).

Building on our prior work, we aimed to confirm that the FKBP12^{F36V}-KRAS^{G12V} protein is functional and that it elicits comparable oncogenic responses to untagged KRAS^{G12V} *in vitro* and *in vivo*. We first utilized NIH/3T3 cells, a commonly used model for testing oncogenic driver genes, and expressed GFP or FKBP12^{F36V}-GFP as controls (**Figure 1B**), as well as KRAS^{G12V} and FKBP12^{F36V}-KRAS^{G12V} (**Figure 1C**). The FKBP12^{F36V}-GFP and FKBP12^{F36V}-KRAS^{G12V} fusions also include HA-tags to facilitate monitoring of GFP and KRAS^{G12V} levels. Importantly, comparable hyperactivation of phosphorylated MEK (pMEK), a key component of oncogenic KRAS^{G12V} downstream signaling, was observed upon the expression of KRAS^{G12V} and FKBP12^{F36V}-KRAS^{G12V} (**Figure 1C**). We next confirmed the effectiveness of the recruitment of VHL to degrade FKBP12^{F36V}-GFP or FKBP12^{F36V}-KRAS^{G12V} and reverse these responses. We observed that dTAG^{V}-1 treatment resulted in the robust degradation of FKBP12^{F36V}-GFP (**Figure 1, B and C**) and FKBP12^{F36V}-KRAS^{G12V} (**Figure 1C**), with no impact on untagged GFP or KRAS^{G12V} levels, highlighting the specificity of dTAG^{V}-1 towards FKBP12^{F36V}-tagged fusions. The degradation of FKBP12^{F36V}-KRAS^{G12V} rapidly reversed this aberrantly activated pMEK response back to baseline levels (**Figure 1C**). Furthermore, dTAG^{V}-1-NEG, a control dTAG molecule that can bind to FKBP12^{F36V} but not recruit VHL, did not degrade FKBP12^{F36V}-GFP or FKBP12^{F36V}-KRAS^{G12V} or alter pMEK levels (**Figure 1, B and C**).

Next, we evaluated the oncogenic potential KRAS^{G12V} or FKBP12^{F36V}-KRAS^{G12V} *in vitro* and *in vivo*. While NIH/3T3 cells expressing GFP or FKBP12^{F36V}-GFP were unable to proliferate as 3D-spheroids, expression of KRAS^{G12V} or FKBP12^{F36V}-KRAS^{G12V} led to 3D-spheroid formation and a significant growth advantage compared with their counterparts *in vitro* (**Figure 1D**). There was no difference in the kinetics of 3D-spheroid formation between KRAS^{G12V} and FKBP12^{F36V}-KRAS^{G12V} *in vitro* (**Figure 1D**). To further examine their tumorigenesis *in vivo*, NIH/3T3 cells expressing KRAS^{G12V} or FKBP12^{F36V}-KRAS^{G12V} cells were injected subcutaneously into the flank of mice and tumor volumes were measured. Consistently, the kinetics of tumorigenesis were comparable between KRAS^{G12V} and FKBP12^{F36V}-KRAS^{G12V} *in vivo*, supporting that the FKBP12^{F36V}-tag did not alter KRAS^{G12V} function (**Figure 1E**). Importantly, dTAG^{V}-1 treatment robustly diminished the proliferation and viability of NIH/3T3 cells expressing FKBP12^{F36V}-KRAS^{G12V} (**Figure 1F**). With

our goal to evaluate targeted KRAS^{G12V} degradation in lung cancer models, we next confirmed these observations in human lung epithelial cells (AALE) (**Supplemental Figure 1B**). We have previously shown that KRAS^{G12V} transforms AALE cells and increases pMEK levels (41, 42). Similar to the results with NIH/3T3 cells, compared to FKBP12^{F36V}-GFP, we observed that the expression of FKBP12^{F36V}-KRAS^{G12V} in AALE cells led to elevated pMEK and the formation of 3D-spheroids (**Supplemental Figure 1, B** and **C**). Pronounced degradation of FKBP12^{F36V}-KRAS^{G12V} was observed upon treatment with dTAG^{V}-1, leading to a reversal of pMEK back to baseline and diminished proliferation as 3D-spheroids (**Supplemental Figure 1, B** and **D**). Together, these results support that the FKBP12^{F36V}-tag did not affect the functionality of the oncoprotein or alter the kinetics of KRAS^{G12V}-induced tumorigenesis and validate the effectiveness of targeted degradation of FKBP12^{F36V}-KRAS^{G12V} by dTAG^{V}-1.

These results motivated our development of a transgenic lung cancer mouse model that enables specific degradation of FKBP12^{F36V}-KRAS^{G12V} using dTAG^{V}-1. We first designed a targeting vector that included a PGK promoter and Lox-Stop-Lox cassette to allow for temporal and spatial control of gene expression as we previously described (43) (**Figure 2A**). The transgene expression is controlled by the Lox-Stop-Lox cassette which can be removed by Cre recombinase. *FKBP12^{F36V}-KRAS^{G12V}* complementary DNA was cloned into the targeting vector (**Figure 2A**). We also included HA-tags to enable monitoring of KRAS^{G12V} levels. After the targeting vector was electroporated into mouse embryonic stem (ES) cells, these cells were engineered to allow single-copy transgene insertion at the *Col1A1* locus. Mouse ES clones that carry the *FKBP12^{F36V}-KRAS^{G12V}* transgene were selected, expanded, and used to inject into C57BL/6 (B6) blastocysts, which gave rise to chimeras (**Figure 2A**). The chimeras were bred with wild type B6 mice, and transgene-positive mice were genotyped, sequenced, and expanded for experiments (**Figure 2B**).

We next sought to examine whether a single allele of *FKBP12^{F36V}-KRAS^{G12V}* would give rise to lung adenocarcinoma modeling human disease in this model. *FKBP12^{F36V}-KRAS^{G12V}* mice were induced by intranasal adenovirus-carrying Cre recombinase delivery at 6 to 8 weeks of age. Starting from 12 to 14 weeks after the induction, *FKBP12^{F36V}-KRAS^{G12V}* mice had visible lung tumors detected by MRI (**Figure 2C**). We then harvested mouse lungs from these *FKBP12^{F36V}-KRAS^{G12V}* tumor-bearing mice to perform histologic analysis. Hematoxylin and eosin (H&E) staining revealed the morphology of tumors formed by *FKBP12^{F36V}-KRAS^{G12V}* cells resembled differentiated adenocarcinomas showing nuclear pleomorphisms including enlarged nuclei with prominent nucleoli (**Figure 2D**) (44). Immunohistochemistry (IHC) staining of lung adenocarcinoma-specific marker, TTF-1, demonstrated strong nuclear expression further confirming primary pulmonary adenocarcinoma (**Figure 2D**). Our *FKBP12^{F36V}-KRAS^{G12V}* mouse strain developed lung adenocarcinoma with complete penetrance and a consistent latency period, comparable to previously reported *KRAS^{G12V}* models (32-35). In summary, we successfully established an *FKBP12^{F36V}-KRAS^{G12V}* GEMM modeling the development of lung adenocarcinoma and can be utilized for targeted degradation using the dTAG system.

dTAG^{V}-1 effectively degrades KRAS^{G12V} and abolishes tumor growth in a *KRAS^{G12V}* GEMM.

We next focused on evaluating the acute and prolonged responses to dTAG-mediated degradation of FKBP12^{F36V}-KRAS^{G12V}. Based on our prior PK and PD studies (28), we treated a cohort of *FKBP12^{F36V}-KRAS^{G12V}* tumor-bearing mice with 35 mg/kg of dTAG^{V}-1 continuously for five days (formulation described in Supplemental Methods and performed as previously described (28)), harvested tumor nodules, and evaluated FKBP12^{F36V}-KRAS^{G12V} degradation by monitoring the HA-tag and downstream signaling (**Figure 3A**). Notably, we observed robust degradation of FKBP12^{F36V}-KRAS^{G12V}, with a concomitant decrease in downstream pERK signaling by western blotting and IHC staining (**Figure 3, B-D**). To examine the duration of FKBP12^{F36V}-KRAS^{G12V} degradation *in vivo*, we treated a separate cohort of tumor-bearing mice with dTAG^{V}-1

continuously for five days. We then stopped compound administration and harvested tumors on days 5 (2 hours after the last dose), 6, 7, and 8. Effective FKBP12^{F36V}-KRAS^{G12V} degradation lasted for 72 hours following the last administration before returning to levels comparable to the vehicle group (**Figure 3B** and **Supplemental Figure 2A**). These results demonstrate successful target engagement and durable degradation of FKBP12^{F36V}-KRAS^{G12V} by dTAG^{V}-1. Furthermore, we examined the antiproliferative and apoptotic effects upon abrupt FKBP12^{F36V}-KRAS^{G12V} loss after five days of dTAG^{V}-1 treatment. IHC staining of the proliferation marker Ki-67 and apoptosis marker cleaved caspase-3 showed that dTAG^{V}-1 led to a significant decrease in Ki-67 levels and an increase in cleaved caspase-3 levels (**Figure 3, E** and **F and Supplemental Figure 2B**). We next investigated the effects of acute FKBP12^{F36V}-KRAS^{G12V} degradation on extracellular matrix component collagen using Masson's trichrome staining. Interestingly, dTAG^{V}-1 treatment caused a reduction in collagen matrices in tumor-bearing lungs (**Supplemental Figure 2, C and D**), suggesting a potential effect on tumor microenvironment upon FKBP12^{F36V}-KRAS^{G12V} degradation.

After confirming that dTAG^{V}-1 successfully degraded FKBP12^{F36V}-KRAS^{G12V} and inhibited oncogenic *KRAS* signaling, we proceeded to assess its impact on tumor growth in vivo. For this, a separate cohort of *FKBP12^{F36V}-KRAS^{G12V}* GEMM mice was induced, and their tumor volumes were monitored and quantified using MRI. Once tumor volumes reached approximately 100 mm^3, mice were randomized into vehicle or dTAG^{V}-1 treatment groups (**Figure 4A**). All mice in the vehicle group displayed aggressive disease progression after a 3-week period (**Figure 4, B** and **C**). In contrast, mice treated with dTAG^{V}-1 showed a significant tumor response (**Figure 4, B and C**), with MRI imaging revealing a reduction in tumor burden of over 50% in all treated mice after long-term treatment by week 3 or week 4 (**Figure 4C**). Importantly, FKBP12^{F36V}-KRAS^{G12V} degradation upon dTAG^{V}-1 administration dramatically increased the survival of tumor-bearing mice (**Figure 4D**). These results indicate that KRAS^{G12V} degradation by dTAG^{V}-1 substantially reduces tumor growth and prolongs survival in the *KRAS^{G12V}*-driven lung cancer model.

To extend these findings, we sought to validate the *in vivo* antitumor effects of KRAS^{G12V} degradation in pancreatic cancer. To do so, we utilized an isogenic pancreatic ductal adenocarcinoma cell line (PATU-8902 FKBP12^{F36V}-KRAS^{G12V}; *KRAS$^{-/-}$*) that we previously developed to study KRAS^{G12V} degradation *in vitro* (29). We injected these cells subcutaneously into the flank of nude mice. Once tumor volume reached approximately 100 mm^3, mice were randomized to either vehicle or dTAG^{V}-1 treatment. Consistent with the results in our lung cancer GEMM, degradation of KRAS^{G12V} upon administration of dTAG^{V}-1 significantly inhibited tumor growth of PATU-8902 FKBP12^{F36V}-KRAS^{G12V}; *KRAS$^{-/-}$* cells (**Figure 4, E and F**). Collectively, these findings validate the efficacy of KRAS^{G12V} degradation across different types of cancer and support targeted degradation as an effective therapeutic strategy.

KRAS^{G12V} degradation drives antitumor immunity through increasing CD8$^+$ T activity.

Previous research has shown that KRAS inhibitors (AMG-510 and MRTX849) induce a pro-inflammatory TME and achieve durable responses alone or in combination with immune checkpoint inhibitors in pre-clinical mouse models (6, 45, 46). To investigate the immune stimulatory effects of targeted degradation of KRAS^{G12V} *in vivo*, we profiled phenotypic and functional alterations of CD8$^+$ T cells following a 5-day treatment with either vehicle or dTAG^{V}-1 in tumor-bearing mice (**Figure 5A**). T cells with high CD44 expression (effector/memory marker) are characterized as effector cells, whereas T cells with high CD62L (naïve T cell marker) are characterized as naïve cells. Profiling of CD8$^+$ T cells showed an increase of CD44^{high} effector CD8$^+$ T cells and a decrease in CD62L^{high} naïve CD8$^+$ T cells upon KRAS^{G12V} degradation (**Figure 5, B** and **C**). To further assess the activation of CD8$^+$ T cells, we analyzed the expression of an activation/co-stimulatory marker, CD69. KRAS^{G12V} degradation led to significantly higher frequencies of CD69$^+$CD8$^+$ T cells (**Figure 5, D** and **E**). Additionally, we evaluated the activity of

cytotoxic T lymphocytes (CTLs) by staining for Granzyme B (GzmB), a cytotoxic granule protein secreted by $CD8^+$ T cells. An increase in $GzmB^+$ $CD8^+$ T cells was observed upon $FKBP12^{F36V}$-$KRAS^{G12V}$ degradation, suggesting an enhanced cytotoxic T cell-mediated clearance of tumor cells (**Figure 5, D** and **E**). These findings suggest that $KRAS^{G12V}$ degradation stimulates a robust antitumor immune program, potentially driven by activated $CD8^+$ T cells.

Transcriptomic analysis reveals that $KRAS^{G12V}$ degradation triggers immune response signaling.

To explore how $KRAS^{G12V}$ degradation affects immune response signaling *in vivo*, we performed a transcriptomic analysis on tumor nodules from mice treated with either vehicle or $dTAG^V$-1 for 5 days (**Supplemental Figure 3A**). Gene set enrichment analysis (GSEA) of differentially expressed genes ($dTAG^V$-1 versus vehicle) identified the most modulated pathways (**Supplemental Figure 3B**). $FKBP12^{F36V}$-$KRAS^{G12V}$ degradation led to the downregulation of genes associated with the cell cycle (**Supplemental Figure 3, B-D**), E2F targets (**Supplemental Figure 3, E** and **F**) and mitosis (**Supplemental Figure 3, G** and **H**). Notably, $FKBP12^{F36V}$-$KRAS^{G12V}$ degradation led to the upregulation of pathways associated with the inflammatory response, interferon gamma response, interferon alpha response, and allograft rejection (**Supplemental Figure 3, I-L**). Heatmaps for the most differentially regulated genes in these top signatures induced upon $FKBP12^{F36V}$-$KRAS^{G12V}$ degradation showed an increased expression of numerous central pro-inflammatory cytokines and chemokines, including *Tnf*, *Cxcl10* and *Ccl5* (**Supplemental Figure 3M**). These factors secreted in the TME can potentially contribute to an optimal antitumor T cell response. To confirm these findings, we then sought to measure the expression of *CCL5*, *CXCL10* and *TNF* upon $dTAG^V$-1 treatment in AALE cells expressing $FKBP12^{F36V}$-$KRAS^{G12V}$ using quantitative reverse transcription-polymerase chain reaction (qRT-PCR). $dTAG^V$-1 treatment significantly upregulated *CCL5* and *CXCL10*, with a trend towards increased TNF expression (**Supplemental Figure 3N**). Furthermore, our RNA-seq data also demonstrated that $FKBP12^{F36V}$-$KRAS^{G12V}$ degradation increased the expression of numerous granzyme subfamily members, including *Gmza*, *Gzmb*, *Gzmc*, as well as *Prf1* and *Ifng* (**Supplemental Figure 3M**), which are crucial for $CD8^+$ T cell-mediated cytotoxicity. These results, in line with immune profiling data, support the immune-stimulatory effects of $KRAS^{G12V}$ degradation.

$KRAS^{G12V}$ degradation reprograms the TME to enhance antitumor immunity.

We next performed single-cell RNA-sequencing (scRNA-seq) to systematically examine the impact on the TME upon degradation of $KRAS^{G12V}$. Lung tumors were collected after 5 days of treatment with either vehicle or $dTAG^V$-1 to degrade $FKBP12^{F36V}$-$KRAS^{G12V}$ in tumor-bearing mice. We collected single suspension cells and sequenced them on the 10X Genomics platform. In total, we obtained single-cell transcriptomes for 11,011 cells from the vehicle group and 7,486 cells from the $dTAG^V$-1 cohort. Using unsupervised clustering, we identified approximately 14 distinct cell clusters according to the gene expression signatures (**Figure 6A** and **Supplemental Figure 4A**). We annotated these clusters with canonical cell type markers and identified tumor cells expressing *Epcam* and *Nkx2-1*, B cells expressing *Cd19*, T cells expressing *Cd3d*, and NK cells expressing *Ncr1*. We also identified various myeloid populations, including monocytes, classical dendritic cells (cDCs), plasmacytoid DCs (pDCs) (marked by *Siglech*, *Bst2* and *Tlr7*), monocyte-derived dendritic cells (marked by *Itgax*, *Flt3* and *Mgl2*), macrophages (both M1-like and M2-like) and neutrophils (*S100a8*) (**Figure 6B** and **Supplemental Figure 4A**).

To dissect the TME alterations following $KRAS^{G12V}$ degradation, we analyzed the immune cell subpopulations. In comparison to the vehicle cohort, $dTAG^V$-1 administration slightly increased the overall frequency of total immune cell populations (**Supplemental Figure 4B**). There was a modest increase in the frequency of T cells, moDCs, NK cells, as well as innate lymphoid cells

(ILC) upon FKBP12^{F36V}-KRAS^{G12V} degradation (**Figure 6C**). Conversely, a decrease in the percentages of B cells and monocytes was observed upon FKBP12^{F36V}-KRAS^{G12V} degradation (**Figure 6C**). Macrophages are broadly classified into two main phenotypes based on their activation states: classically activated (M1) and alternatively activated (M2) (47, 48). While M1-like macrophages can exert antitumor effects, M2-like macrophages often contribute to tumor growth and immune evasion (47, 48). Consistent with previous studies in the murine and human lung tumors (49, 50), the macrophages in the lung TME largely belong to the M2-like macrophages, expressing *Chil3* and *Mrc1* (**Supplemental Figure 4A**). Notably, our scRNA-seq analysis revealed that dTAG^{V}-1 treatment led to an increase of M1-like macrophages expressing *Ccl3*, *Tnf*, *Ler3*, *Clec4n*, *Tlr2/4* and Cd80 (51), whereas a decrease in M2-like macrophages expressing *Chil3* and *Mrc1* was observed (**Figure 6C** and **Supplemental Figure 4A**). The reduction in M2-like macrophages was further validated by IHC staining of MRC1 (CD206) in the lung tumors upon FKBP12^{F36V}-KRAS^{G12V} degradation (**Supplemental Figure 4, C** and **D**). These findings suggest that KRAS^{G12V} degradation might have an impact on promoting tumor-associated macrophages towards an M1-like antitumor phenotype. Given the high degree of heterogeneity and plasticity of macrophages, further investigation and functional validation are warranted in future work.

In addition, accumulating evidence indicates that B cells are strongly enriched in the TME in both murine tumor models as well as human lung cancer patients (49, 52-54). In agreement with this, our scRNA-seq analysis revealed B cells constitute a major immune cell population infiltrating in the murine KRAS^{G12V} tumors. Unsupervised clustering of B cells identified four distinct clusters (**Supplemental Figure 4E**). Consistent with recent findings (52), most tumor-infiltrating B cells are in cluster 1, which exhibits a highly activated phenotype, expressing *Cd86* and *Cxcr4*. Cluster 2 B cells, expressing *Fcrl5*, display a memory-like phenotype (55, 56) (**Supplemental Figure 4F**). Cluster 3 B cells, expressing *Hspa1a*, *Hspa1b*, and *Jun*, are associated with an activated phenotype, whereas cluster 4, which is the smallest group, shows high expression of *Iglc1* (**Supplemental Figure 4F**). Interestingly, FKBP12^{F36V}-KRAS^{G12V} degradation led to a decrease in the percentage of cluster 1 B cells compared to the vehicle group, while the frequency of cluster 3 B cells increased (**Supplemental Figure 4G**). The percentages of clusters 2 and 4 remained similar upon FKBP12^{F36V}-KRAS^{G12V} degradation. These observations suggest that KRAS^{G12V} degradation differentially affects various subtypes of activated B cells, which merits further investigation in the future.

Our *in vivo* immune profiling analysis suggested that KRAS^{G12V} degradation increased CD8^{+} T cell activity in the TME. To comprehensively characterize the T-cell subpopulations induced upon FKBP12^{F36V}-KRAS^{G12V} degradation, we further analyzed the scRNA-seq dataset and performed unbiased clustering of T cells. This approach identified 6 major clusters defined by the expression of marker genes, suggesting heterogeneous and complex populations. In the CD8^{+} T-cell populations, cells with a high level of *Sell* and low levels of *Cd44* and *Ifng* are consistent with naïve and inactivated states and were thus classified as 'CD8^{+}-naïve' cluster. FKBP12^{F36V}-KRAS^{G12V} degradation reduced the percentage of naïve CD8^{+} cells (**Figure 6, D-F**). Cells in clusters with high *Ifng* and *Cd44* resemble cytotoxic T cells and effector T cells, which were therefore classified as 'CD8^{+}-effector and cytotoxic T cells'. FKBP12^{F36V}-KRAS^{G12V} degradation caused an increase in the effector and cytotoxic CD8^{+} T cells (**Figure 6, D-F**). Additionally, in the CD4^{+} T-cell populations, we also observed a similar trend of decreased CD4^{+}-naïve T cells and increased CD4^{+}-effector T cells (**Figure 6, D-F**). Our unbiased clustering also identified CD4^{+} T_{regs}, which express high levels of *Foxp3* (**Figure 6, D-F**). An increase in the frequency of CD4^{+} T_{regs} was seen upon FKBP12^{F36V}-KRAS^{G12V} degradation, which might indicate potential feedback from increased effector and cytotoxic T cell activity.

To complement our scRNA-seq findings of immune TME alterations, we performed multiplex immunofluorescence (IF) analysis on lung tumors from mice that were subjected to a 5-day treatment with either vehicle or dTAG^{V}-1 (**Figure 7, A-C**). Consistently, an increase of CD3^{+} T cells was observed upon abrupt loss of FKBP12^{F36V}-KRAS^{G12V}, compared with vehicle (**Figure 7, A** and **C**). Likewise, dTAG^{V}-1 treatment also led to a higher percentage of Foxp3^{+} T_{regs} (**Figure 7, A** and **C**). In addition, similar to our observations using scRNA-seq analysis, IF imaging showed that the frequency of CD19^{+} B cells was decreased upon FKBP12^{F36V}-KRAS^{G12V} degradation (**Figure 7, B** and **C**).

In summary, in line with the *in vivo* immune profiling and bulk transcriptomic analysis, our scRNA-seq analysis complemented with multiplex IF imaging confirms an antitumor immune response following dTAG^{V}-1 treatment to degrade FKBP12^{F36V}-KRAS^{G12V}. These alterations include (1) slightly increasing overall immune cell infiltration, (2) decreasing M2-like and increasing M1-like macrophages, (3) decreasing B cells, (4) reducing the naïve CD8^{+} and CD4^{+} T cells, and (5) increasing the effector and cytotoxic CD8^{+} T cells. These data further support the beneficial effects of targeted degradation of KRAS^{G12V} in rewiring the TME to enhance antitumor immunity.

Antitumor immunity by KRAS^{G12V} degradation is partly dependent on CD8^{+} T cells.

Our integrated analysis above demonstrated that the antitumor immunity by KRAS^{G12V} degradation centered on T cells. To determine whether CD8^{+} or CD4^{+} T cells directly contribute to antitumor response by dTAG^{V}-1 treatment, we assessed the impact of perturbing immune cell function by *in vivo* neutralization antibodies against CD8 (anti-CD8) or CD4 (anti-CD4) (**Supplemental Figure 5**). FKBP12^{F36V}-KRAS^{G12V} tumor-bearing mice were randomized to dTAG^{V}-1 treatment or combining dTAG^{V}-1 with either anti-CD8 or anti-CD4. Notably, compared with non-depletion of T cells mice in the dTAG^{V}-1 group, CD8^{+} T cell-depleted mice had significantly higher tumor burdens (**Figure 7, D-F**). Interestingly, no significant difference was observed between non-depletion mice and CD4^{+} T cell-ablated mice (**Figure 7, D-F**). These findings suggest depleting CD8^{+} but not CD4^{+} T cells mitigated the antitumor effect of FKBP12^{F36V}-KRAS^{G12V} degradation by dTAG^{V}-1, highlighting antitumor immunity by KRAS^{G12V} degradation is partly dependent on CD8^{+} T cells.

In summary, our work offers valuable insights into how KRAS^{G12V} degradation influences both tumor progression and the immune response, underscoring degraders as a potent strategy for targeting *KRAS* mutant cancers. Furthermore, our study highlights the potential of the dTAG system in developing GEMMs for the study and validation of drug targets.

Discussion

Targeted protein degradation holds incredible promise as a therapeutic strategy in diseases including cancer (14-17, 57). There is a current lack of targeted degradation strategies to study the consequences of drug target loss *in vivo*. Here, we focused on $KRAS^{G12V}$, which is the second most common mutation in NSCLC and a driver in several cancers including pancreatic and colorectal cancer (58, 59). While breakthroughs in the development of $KRAS^{G12C}$ inhibitors including AMG-510 (Sotorasib) (9, 10, 60) and MRTX849 (Adagrasib) (61) represent a paradigm shift in the clinical management of NSCLC patients harboring a $KRAS^{G12C}$ mutation, there is currently a lack of selective $KRAS^{G12V}$ inhibitors. As the field moves towards targeting other additional KRAS mutants, an improved understanding of targeting $KRAS^{G12V}$ *in vivo* is necessary. We aimed to advance the dTAG system to generate a degradable cancer GEMM using $KRAS^{G12V}$ as a prioritized target.

In this study, we demonstrate that this mouse model harboring a tagged allele of $KRAS^{G12V}$ recapitulates the development of human adenocarcinoma. Our $FKBP12^{F36V}$-$KRAS^{G12V}$ mouse strain develops lung adenocarcinoma with complete penetrance and a consistent latency period, comparable to previously reported $KRAS^{G12V}$ models (32-35). Critically, treatment with dTAG molecules effectively models the impact of targeted degradation of $KRAS^{G12V}$. In the mice, $dTAG^{V}$-1 administration led to robust and durable degradation of $KRAS^{G12V}$, along with pronounced inhibition of downstream signaling, consistent with previous findings from studies using KRAS inhibitors in murine cancer models (6, 7). Strikingly, $dTAG^{V}$-1 considerably reduced tumor growth in all treated $KRAS^{G12V}$ mice and the $FKBP12^{F36V}$ tag did not affect the kinetics of $KRAS^{G12V}$ transformation nor tumorigenesis *in vitro* and *in vivo*. Furthermore, while we focused on developing an NSCLC GEMM, our incorporation of *Cre*-recombinase-mediated introduction of $FKBP12^{F36V}$-$KRAS^{G12V}$ supports similar application in other tissues and cancers of interest including pancreatic cancer. Towards this aim, we performed experiments that extend into pancreatic cancer and demonstrate that $dTAG^{V}$-1-mediated $KRAS^{G12V}$ degradation drastically inhibited tumor growth in the PATU-8902 pancreatic cancer model. Our study demonstrates the unique power of these mouse models for *in vivo* evaluation of the effects of $KRAS^{G12V}$ degradation on tumorigenesis.

Importantly, our GEMM enables the evaluation of responses in an immune-competent mouse, which led us to test whether degrading $KRAS^{G12V}$ leads to an increased immune response *in vivo*. Prior work has linked $KRAS^{G12C}$ inhibition to an immune response (46). In preclinical studies, treatment with AMG-510 showed a pro-inflammatory TME and induced durable cures alone, and in combination with immune-checkpoint inhibitors (6). Likewise, MRTX849 demonstrated an enhanced antitumor immunity, partly through increased MHC class I protein expression and decreased levels of immunosuppressive factors (45). MRTX849 also sensitized tumors to immune-checkpoint inhibitors (45). Like these observations, we found that $KRAS^{G12V}$ degradation drove antitumor immunity by increasing $CD8^{+}$ T cell activity. This was further manifested by a substantial increase of $CD44^{high}$ effector $CD8^{+}$ T cells, as well as $CD69^{+}$ $CD8^{+}$ and $GzmB^{+}$ $CD8^{+}$ cytotoxic T cells. Complementing these immune profiling data, our transcriptomic analysis revealed that $KRAS^{G12V}$ degradation causes a strong inhibition of KRAS-dependent downstream signaling (E2F, mitosis, and cell cycle pathways) while also triggering robust immune response signaling.

Given our limited understanding of how $KRAS^{G12V}$ impacts the lung TME, we conducted scRNA-seq analysis to identify global alterations in the TME following $KRAS^{G12V}$ degradation. This analysis was complemented with further IHC and multiplex imaging staining. Our study uncovered several key observations and mechanisms of action on immune components. $KRAS^{G12V}$ degradation upon $dTAG^{V}$-1 administration: (1) triggers the expansion and reduction of certain subtypes of tumor-infiltrating lymphoid (T and B cells) and myeloid cells (M1-like and M2-like

macrophages and DCs), (2) promotes a shift of naïve $CD4^+$ and $CD8^+$ T cells to effector/activated T cells, and cytotoxic $CD8^+$ T cells, and (3) elicits an increase in the expression of an antitumor cytotoxic gene signature. Supporting this, our *in vivo* T cell depletion assays support that a functional immune system centered on $CD8^+$ T cells is required for the antitumor response induced upon $KRAS^{G12V}$ degradation. Additionally, our results also indicate that $KRAS^{G12V}$ degradation may promote tumor-associated macrophages towards M1-like antitumor phenotype and affect different subtypes of B cells, which merits further investigation. Notably, there is emerging interest in utilizing covalently modified peptide/MHC class I complexes as tumor-specific neoantigens with $KRAS^{G12C}$ inhibitors (62, 63). Future work is necessary to examine whether KRAS degradation promotes the production of neoantigen peptides and whether this phenomenon contributes to antitumor immunity. This research will also help experimentally rule out the possibility of an $FKBP12^{F36V}$ tag-induced immune response.

Our study also expands the use of the dTAG system for *in vivo* modeling. We and others have shown that the dTAG system can be employed in xenograft models (27, 28, 37, 40, 64, 65) and mouse models of embryonic development (38). An important consideration in these efforts is to ensure that the tagged protein is functional and maintains the expected level of expression. One limitation of tag-based systems is that the addition of a tag has the potential to alter protein stability and half-life (66). In GEMMs, endogenous fusion with the $FKBP12^{F36V}$-tag may impact protein stability and half-life, decreasing protein expression *in vivo* (39, 67). In our oncogene-induction model, $FKBP12^{F36V}$-$KRAS^{G12V}$ is driven by a PGK promoter. Studies in embryonic development suggest that this may be target-specific (38) but future work is warranted to improve tagging strategies to maintain protein stability to address this limitation. Furthermore, our oncogene-induction model does not allow for the evaluation of the tolerability of systemic KRAS degradation. GEMMs that employ the dTAG system such as those recently described for CDK2 and CDK5 will prove to be highly complementary for evaluating toxicities from specific target protein loss (39).

In line with other studies, this work provides pre-clinical support that targeted degradation is a powerful strategy to target mutant KRAS *in vivo* (21-25, 68). Recently, a clinical $KRAS^{G12D}$ degrader (ASP3082) was described to have potent antitumor activities in multiple *G12D*-driven mouse models including pancreatic, colorectal, and NSCLC cancer (26). Currently, a phase 1 clinical trial is underway in patients with previously treated, locally advanced, or metastatic solid tumors with $KRAS^{G12D}$ mutation (NCT05382559). While it remains an open question whether KRAS degradation will provide a benefit over inhibition, our work highlights the therapeutic potential of targeted degradation of KRAS. It is worth noting that due to the current unavailability of $KRAS^{G12V}$-specific inhibitors, a direct comparison of the immunological effects between degrading $KRAS^{G12V}$ and inhibiting $KRAS^{G12V}$ is not yet experimentally achievable. When these inhibitors become available, our mouse model will serve as an important platform for evaluating the differential effects on downstream signaling, tumorigenesis, and TME alterations, allowing for a comprehensive comparison of the responses to inhibitors and degraders. With the emergence of pan-KRAS and RAS(ON) multi-selective inhibitors (69-72), it will also be interesting to evaluate the immune responses triggered by these inhibitors and $dTAG^V$-1-mediated degradation in our model.

Interestingly, a recent study showed that *Kras* oncogene ablation could prevent resistance to KRAS inhibitors in advanced lung adenocarcinomas, supporting the potential benefit of protein degradation (34). Supported by our prior cellular studies using the dTAG system studying resistance mechanisms to targeted agents (28, 73), we expect that our model will enable the identification of resistance mechanisms to KRAS disruption and the testing of drug combination strategies *in vivo*. Future work will be necessary to evaluate drug combination approaches and to extend our model to additional *KRAS* mutants and other *KRAS*-driven cancers. In summary, our study demonstrates that degrading $KRAS^{G12V}$ drives antitumor immunity and abolishes tumor

growth in lung cancer. Our work highlights the value of degradable model systems to understand and advance targeted degradation strategies as cancer therapeutics.

Methods

Sex as a biological variable

Our study examined male and female animals, and similar findings are reported for both sexes.

Generation of FKBP12^{F36V}-KRAS^{G12V} transgenic mice

To generate FKBP12^{F36V}-KRAS^{G12V} mice that enable specific degradation by dTAG^{V}-1, we designed a targeting vector with a PGK promoter and Lox-Stop-Lox cassette, which allows the temporal and spatial control of gene expression as we previously described (43). *FKBP12^{F36V}-KRAS^{G12V}* complementary DNA was cloned into the targeting vector. The transgene expression is controlled by the stop cassette which can be removed by Cre recombinase. After the targeting vector was electroporated into embryonic stem (ES) cells, these cells were engineered to allow single-copy transgene insertion at the *Co1IA1* locus. ES clones that carry the *FKBP12^{F36V}-KRAS^{G12V}* transgene were selected, expanded, and used to inject into B6 blastocysts, which gave rise to chimeras. The chimeras were bred with wild-type B6 mice, and transgene-positive mice were genotyped/sequenced and expanded for experiments. From 6 to 8 weeks of age, mice were induced with adenovirus-SPC-Cre recombinase (Ad-Cre) by intranasal intubation to allow Cre-lox-mediated recombination.

In vivo studies

For NIH/3T3 KRAS^{G12V} or FKBP12^{F36V}-KRAS^{G12V} mouse model studies, 1 x 10^6 cells were injected into the flank of nude mice. Tumor growth was monitored and measured by caliper. For treatment studies using *FKBP12^{F36V}-KRAS^{G12V}* GEMMs, mice were evaluated by MRI imaging (Preclinical Imaging Laboratory, NYU Grossman School of Medicine and *in vivo* Imaging Facility, University of Pittsburgh UPMC Hillman Cancer Center) to quantify lung tumor burden before randomization and after drug treatment. Once the tumor volumes reached approximately 100 mm^3 (quantified by 3D-slicer using MRI images), the mice were then enrolled and randomized into either vehicle or dTAG^{V}-1 (35 mg/kg). For treatment studies using the PATU-8902 pancreatic cancer model, 1 x 10^6 cells were injected into the flank of nude mice. Tumor volumes were monitored and measured by caliper before randomization. Once tumor volumes reached approximately 100 mm^3, mice were randomized to treatment with either vehicle or dTAG^{V}-1 (35 mg/kg). For CD8$^+$ or CD4$^+$ T cell depletion studies, mice were injected intraperitoneally with either anti-CD8 antibody (400 mg, Bio X Cell, clone 2.43), or anti-CD4 (400 mg, Bio X Cell, clone GK1.5), or isotype control 48 and 24 h before beginning dTAG^{V}-1 treatment, and every 4 days thereafter.

Illustration tool

The schematic images were created with BioRender (BioRender.com).

Statistics

Statistical analyses were performed using GraphPad Prism v10 software and statistical significance was determined by $P < 0.05$. Data are presented as mean with SD unless otherwise specified. Statistical comparisons for two groups were performed using a two-tailed Student's *t*-test and multiple comparisons were performed using one-way ANOVA followed by post hoc Dunnett's test or Tukey's test unless otherwise specified (*$P < 0.05$, **$P < 0.01$, ***$P < 0.001$, ****$P < 0.0001$).

Study approval

All animal studies were reviewed and approved by the Institutional Animal Care and Use Committee at NYU Grossman School of Medicine and University of Pittsburgh School of Medicine. Both male and female mice were used, and all mice were maintained in accordance with NYU Grossman School of Medicine and University of Pittsburgh School of Medicine on the

care, welfare, and treatment of laboratory animals. All experiments met or exceeded the standards of the Association for the Assessment and Accreditation of Laboratory Animal Care, International, the U.S. Department of Health and Human Services, and all local and federal animal welfare laws.

Data availability

The accession number for the raw and processed data of bulk RNA sequencing and single-cell RNA sequencing generated and reported in this paper is GEO: GSE234472. All supporting data are provided in the Supporting Data Values file and available online as Supplemental Material.

Extended material and methods

Additional details on compounds, reagents, assays, and bioinformatic analysis are provided in the Supplemental Methods.

Author contributions

HZ, KKW, and BN conceptualized the study, designed the experiments, interpreted the data, wrote the manuscript, and supervised the study. DL, KG, JG, and SK performed most of the experiments, analyzed and interpreted the data, and contributed to writing the paper. YH performed bioinformatics analyses. ATO, CCK, YP, FS, HK, WMA, YL, TC, CT, MR, MM, DSL, JC, MSDP, JS, AC, JP, XS, ZZ, and MP conducted experiments, including *in vitro* assays in NIH/3T3 and AALE cells, multiplex imaging, MRI scan, dosing and IHC. FL, HH, SG, TZ, BH, BAN, WC, MEK, XW, JL, AHB, YL, XZ, TCB and NSG provided resources, analyzed, and interpreted the data. All authors reviewed the manuscript.

Acknowledgments

The authors thank members of the Zhang, Wong, and Nabet laboratories for feedback on this study and manuscript. We thank Haikuo Zhang for his advice on mouse modeling. This work was supported by: NIH/NCI K22 CA276357 (to HZ), NIH/NCI K22 CA258805 (to BN), NIH/NCI Cancer Center Support Grant P30 CA015704 (to BN), NIH/NCI U01 CA282109 (to BN), and Fred Hutchinson Cancer Center Human Biology Division Pilot Award (to BN and AHB). SG is supported by NIH/NCI K22 CA279077, PhRMA Foundation Faculty Starter Grant. BAN is a Damon Runyon Clinical Investigator supported (in part) by the Damon Runyon Cancer Foundation (CI-124-23). We thank the Experimental Pathology Research Laboratory and the Genome Technology Center, which are partially supported by the NIH/NCI Cancer Center Support Grant P30CA016087 at NYU Langone's Laura and Isaac Perlmutter Cancer Center. We also thank the Preclinical Imaging Laboratory, a shared resource partially supported by the Laura and Isaac Perlmutter Cancer Center Support Grant NIH/NCI 5P30CA016087 and NIBIB Biomedical Technology Resource Center Grant NIH P41 EB017183. This project used the Hillman Animal Facility that is supported in part by award P30CA047904, and utilized the Hillman Cancer Center *In Vivo* Imaging Facility, a shared resource at the University of Pittsburgh supported by the CCSG P30 CA047904. This research was supported by the Genomics & Bioinformatics Shared Resource, RRID:SCR_022606, and Cellular Imaging Shared Resource, RRID:SCR_022609 of the Fred Hutch/University of Washington/Seattle Children's Cancer Consortium (P30 CA015704).

Figure Legends

Figure 1. Validation of targeted degradation of $KRAS^{G12V}$ using the dTAG system. (**A**) Schematic of the dTAG system showing that $dTAG^V$-1 recruits the von Hippel-Lindau (VHL) E3 ubiquitin ligase to induce targeted degradation of $FKBP12^{F36V}$-$KRAS^{G12V}$. (**B**) Representative images of NIH/3T3 cells expressing GFP or $FKBP12^{F36V}$-GFP treated with DMSO, 500 nM $dTAG^V$-1, or 500 nM $dTAG^V$-1-NEG for 8 h. The scale bar represents 20 μm. Data is representative of *n* = 3 independent experiments. (**C**) Immunoblot analysis of HA to detect $FKBP12^{F36V}$-GFP or $FKBP12^{F36V}$-$KRAS^{G12V}$, KRAS, pMEK, MEK, and α-Tubulin of NIH/3T3 cells expressing GFP, $FKBP12^{F36V}$-GFP, $KRAS^{G12V}$, or $FKBP12^{F36V}$-$KRAS^{G12V}$ treated with DMSO, 500 nM $dTAG^V$-1, or 500 nM $dTAG^V$-1-NEG for 8 h. Data is representative of *n* = 3 independent experiments. (**D**) Antiproliferation of NIH/3T3 cells expressing GFP, $FKBP12^{F36V}$-GFP, $KRAS^{G12V}$, or $FKBP12^{F36V}$-$KRAS^{G12V}$ cultured as ultra-low adherent 3D-spheroid suspensions for 144 h. Data is presented as mean ± s.d. of *n* = 20 biologically independent samples and are representative of *n* = 3 independent experiments. RLU = Relative light units. (**E**) Tumor volume changes of NIH/3T3 cells expressing $KRAS^{G12V}$ or $FKBP12^{F36V}$-$KRAS^{G12V}$ that were subcutaneously injected into mice. Data is presented as mean ± SEM from *n* = 10 per group. (**F**) DMSO-normalized proliferation of NIH/3T3 cells expressing $FKBP12^{F36V}$-$KRAS^{G12V}$ cultured as ultra-low adherent 3D-spheroid suspensions and treated with the indicated compounds for 120 h. Data is presented as mean ± s.d. of *n* = 4 biologically independent samples and are representative of *n* = 3 independent experiments. ****$P < 0.0001$ (**D**) and non-significant (NS) (**D-E**) by a one-way ANOVA with post hoc Tukey's test (**D**) or a two-tailed Student's *t*-test (**E**).

Figure 2. Establishing a GEMM for targeted degradation of $KRAS^{G12V}$ in lung cancer. (**A**) Schematic showing the design of the *$FKBP12^{F36V}$-$KRAS^{G12V}$* GEMM. (**B**) Genomic sequencing confirmation of *$KRAS^{G12V}$* mutation in the GEMM. (**C**) MRI was performed to detect lung tumor nodules 12-14 weeks after adenovirus-carrying Cre recombinase delivery. (**D**) Representative images of hematoxylin and eosin (H&E) and immunohistochemistry (IHC) for TTF-1 of lung tumors from the *$FKBP12^{F36V}$-$KRAS^{G12V}$* GEMM. The scale bar represents 500 and 100 μm from top to bottom.

Figure 3. $dTAG^V$-1 effectively degrades $KRAS^{G12V}$ and inhibits downstream signaling in a *$KRAS^{G12}$*-driven lung cancer GEMM. (**A**) Schematic showing the *in vivo* dosing schedule for evaluating target engagement and degradation. Mice were treated once daily with either vehicle or $dTAG^V$-1 (35 mg/kg) for 5 days. (**B**) Immunoblot analysis of HA to detect $FKBP12^{F36V}$-$KRAS^{G12V}$, pERK, ERK, and actin in lung tumor nodules after the indicated treatment and time from *n* = 3-5 per group. (**C**) Representative images of H&E and IHC staining for HA to detect $FKBP12^{F36V}$-$KRAS^{G12V}$ and pERK of lung tumors after the indicated treatment from *n* = 3 per group. The scale bar represents 500, 200, 100 and 50 μm from top to bottom. (**D**) Quantification of HA to detect $FKBP12^{F36V}$-$KRAS^{G12V}$ and pERK positive staining after the indicated treatment. Data is presented as mean ± s.d. of ten representative areas from *n* = 3 mice per group. (**E**) Representative images of IHC staining for Ki-67 and cleaved caspase-3 of lung tumors after the indicated treatment. The scale bar represents 100 and 50 μm for top and bottom. (**F**) Quantification of Ki-67 and cleaved caspase-3 positive staining after the indicated treatment. Data is presented as mean ± s.d. of ten representative areas from *n* = 3 mice per group. ****$P < 0.0001$ (**D** and **F**) by a two-tailed Student's *t*-test.

Figure 4. $KRAS^{G12V}$ degradation abolishes tumor growth in *$KRAS^{G12V}$*-driven murine lung and pancreatic cancer models. (**A**) Schematic showing the *in vivo* dosing schedule for evaluating long-term $dTAG^V$-1 treatment. (**B**) Representative MRI scans (one vehicle and three $dTAG^V$-1 treated mice) of tumor baseline, 2 weeks, and 3 weeks after treatment initiation. The red arrowheads indicate lung tumors, and the red circles indicate the heart. (**C**) Waterfall plot and dot plot showing changes in tumor volume compared to baseline after 2 or 3/4 weeks of treatment.

Data is presented as mean ± s.d. from n = 8 per group. (**D**) Kaplan-Meier survival curve of *FKBP12*^{F36V}-*KRAS*^{G12V} lung cancer mice after long-term treatment with vehicle or dTAG^{V}-1 from n = 9 per group. (**E**) Tumor volume changes of PATU-8902 FKBP12^{F36V}-KRAS^{G12V}; *KRAS*$^{-/-}$ cells that were subcutaneously injected into mice and treated with vehicle or dTAG^{V}-1. Data is presented as mean ± SEM from n = 12 per group. (**F**) Representative pancreatic tumors after the indicated treatment. ****P < 0.0001 by a one-way ANOVA with post hoc Dunnett's test (**C**) and a two-tailed Student's t-test (**E**).

Figure 5. KRAS^{G12V} degradation increases CD8^{+} T activity in a *KRAS*^{G12V}-driven lung cancer GEMM. (**A**) Schematic showing the experimental design for immune profiling. After confirming tumor burden by MRI, mice were randomized and treated once daily with either vehicle or dTAG^{V}-1 (35 mg/kg) for 5 days. Tumor nodules were then collected, and tumor-infiltrating lymphocytes were analyzed by flow cytometry. (**B** and **C**) Frequencies of CD44^{+} CD8^{+} T cells and CD62L^{+} CD8^{+} T cells from n = 5 per group. Data is presented as mean ± SEM (**C**). (**D** and **E**) Frequencies of CD69^{+} CD8^{+} T cells and GZMB^{+} CD8^{+} T cells from n = 5 per group. Data is presented as mean ± SEM (**E**). *P < 0.05 and **P < 0.01 (**C** and **E**) by a two-tailed Student's t-test.

Figure 6. Single-cell RNA-seq reveals KRAS^{G12V} degradation reprograms the TME to promote antitumor immunity in a *KRAS*^{G12V}-driven lung cancer GEMM. (**A**) UMAP plot showing identified cell populations including tumor cells, immune cells, and fibroblasts. (**B**) UMAP plots showing the expression of cell-type specific marker genes. (**C**) Percentage of cells in TME of annotated clusters in response to the indicated treatments. (**D**) UMAP plot showing identified cell subsets in T cell population. (**E**) UMAP plots show the expression of selected marker genes. (**F**) Percentage of cells in the annotated T cell subsets in response to the indicated treatments.

Figure 7. Antitumor immunity by KRAS^{G12V} degradation is partly dependent on CD8^{+} T cells in a *KRAS*^{G12V}-driven lung cancer GEMM. (**A** and **B**) Representative multiplex IF images showing (**A**) tumor infiltrating CD3^{+} T cells, Foxp3^{+} Treg cells and (**B**) CD19^{+} B cells in response to indicated treatment. The same samples are presented in **A** and **B**. The scale bar represents 50 and 10 μm from left to right, respectively. (**C**) Quantification of CD3^{+} T cells, Foxp3^{+} Treg cells and CD19^{+} B cells in response to the indicated treatment. Data is presented as mean ± s.d. of ten representative areas from n = 3 mice per group. (**D**) Representative MRI scans of lung tumors at baseline and 2 weeks in response to indicated treatment. The red arrowheads indicate lung tumors. (**E** and **F**) Waterfall plot (**E**) and dot plot (**F**) showing changes in tumor volume compared to baseline after 2 weeks of treatment. Data is presented as mean ± s.d. from n = 4-6 per group. **P < 0.01, ***P < 0.001, ****P < 0.0001 and non-significant (NS) by a two-tailed Student's t-test (**C**) and a one-way ANOVA with post hoc Tukey's test (**F**).

References

1. Siegel R L, et al. Cancer statistics, 2019. *CA Cancer J Clin.* 2019;69(1):7-34.
2. Cheng L, et al. Molecular pathology of lung cancer: key to personalized medicine. *Mod Pathol.* 2012;25(3):347-369.
3. Scheffler M, et al. K-ras mutation subtypes in NSCLC and associated co-occuring mutations in other oncogenic pathways. *J Thorac Oncol.* 2019;14(4):606-616.
4. Janes M R, et al. Targeting KRAS mutant cancers with a covalent G12C-specific inhibitor. *Cell.* 2018;172(3):578-589 e517.
5. Lanman B A, et al. Discovery of a covalent inhibitor of $KRAS^{G12C}$ (AMG 510) for the treatment of solid tumors. *J Med Chem.* 2020;63(1):52-65.
6. Canon J, et al. The clinical KRAS(G12C) inhibitor AMG 510 drives anti-tumour immunity. *Nature.* 2019;575(7781):217-223.
7. Hallin J, et al. The $KRAS^{G12C}$ inhibitor MRTX849 provides insight toward therapeutic susceptibility of KRAS-mutant cancers in mouse models and patients. *Cancer Discov.* 2020;10(1):54-71.
8. Jänne P A, et al. KRYSTAL-1: activity and safety of adagrasib (MRTX849) in advanced/metastatic non-small cell lung cancer (NSCLC) harboring KRAS G12C mutation. *ENA.* 2020.
9. Hong D S, et al. $KRAS^{G12C}$ inhibition with sotorasib in advanced solid tumors. *N Engl J Med.* 2020;383(13):1207-1217.
10. de Langen A J, et al. Sotorasib versus docetaxel for previously treated non-small-cell lung cancer with $KRAS^{G12C}$ mutation: a randomised, open-label, phase 3 trial. *Lancet.* 2023;401(10378):733-746.
11. Zhao Y, et al. Diverse alterations associated with resistance to KRAS(G12C) inhibition. *Nature.* 2021;599(7886):679-683.
12. Xue J Y, et al. Rapid non-uniform adaptation to conformation-specific KRAS(G12C) inhibition. *Nature.* 2020;577(7790):421-425.
13. Kim D, et al. Targeting KRAS(G12C): from inhibitory mechanism to modulation of antitumor effects in patients. *Cell.* 2020;183(4):850-859.
14. Sakamoto K M, et al. Protacs: chimeric molecules that target proteins to the Skp1-Cullin-F box complex for ubiquitination and degradation. *Proc Natl Acad Sci U S A.* 2001;98(15):8554-8559.
15. Burslem G M, and Crews C M. Proteolysis-targeting chimeras as therapeutics and tools for biological discovery. *Cell.* 2020;181(1):102-114.
16. Bekes M, et al. PROTAC targeted protein degraders: the past is prologue. *Nat Rev Drug Discov.* 2022;21(3):181-200.
17. Chirnomas D, et al. Protein degraders enter the clinic - a new approach to cancer therapy. *Nat Rev Clin Oncol.* 2023;20(4):265-278.
18. Bondeson D P, et al. Catalytic in vivo protein knockdown by small-molecule PROTACs. *Nat Chem Biol.* 2015;11(8):611-617.
19. Burslem G M, et al. The advantages of targeted protein degradation over inhibition: an RTK case study. *Cell Chem Biol.* 2018;25(1):67-77 e63.
20. Koide E, et al. Development and characterization of selective FAK inhibitors and PROTACs with in vivo activity. *Chembiochem.* 2023:e202300141.
21. Zeng M, et al. Exploring targeted degradation strategy for oncogenic $KRAS^{G12C}$. *Cell Chem Biol.* 2020;27(1):19-31 e16.
22. Bond M J, et al. Targeted degradation of oncogenic $KRAS^{G12C}$ by VHL-recruiting PROTACs. *ACS Cent Sci.* 2020;6(8):1367-1375.
23. Popow J, et al. Targeting cancer with small-molecule pan-KRAS degraders. *Science.* 2024;385(6715):1338-1347.

24. Bery N, et al. A potent KRAS macromolecule degrader specifically targeting tumours with mutant KRAS. *Nat Commun.* 2020;11(1):3233.
25. Yang J, et al. A pan-KRAS degrader for the treatment of KRAS-mutant cancers. *Cell Discov.* 2024;10(1):70.
26. Nagashima T, et al. Abstract 5735: Novel KRAS G12D degrader ASP3082 demonstrates in vivo, dose-dependent KRAS degradation, KRAS pathway inhibition, and antitumor efficacy in multiple KRAS G12D-mutated cancer models. *Cancer Research.* 2023;83(7_Supplement):5735.
27. Nabet B, et al. The dTAG system for immediate and target-specific protein degradation. *Nat Chem Biol.* 2018;14(5):431-441.
28. Nabet B, et al. Rapid and direct control of target protein levels with VHL-recruiting dTAG molecules. *Nat Commun.* 2020;11(1):4687.
29. Ferguson F M, et al. Discovery of a selective inhibitor of doublecortin like kinase 1. *Nat Chem Biol.* 2020;16(6):635-643.
30. Nabet B. Charting a new path towards degrading every protein. *Chembiochem.* 2021;22(3):483-484.
31. Nabet B, et al. Protein homeostasis in drug discovery: a chemical biology perspective. *Wiley.* 2022:447-464.
32. Guerra C, et al. Tumor induction by an endogenous K-ras oncogene is highly dependent on cellular context. *Cancer Cell.* 2003;4(2):111-120.
33. Sanclemente M, et al. c-RAF ablation induces regression of advanced Kras/Trp53 mutant lung adenocarcinomas by a mechanism independent of MAPK signaling. *Cancer Cell.* 2018;33(2):217-228 e214.
34. Salmon M, et al. Kras oncogene ablation prevents resistance in advanced lung adenocarcinomas. *J Clin Invest.* 2023;133(7).
35. Drosten M, et al. Genetically engineered mouse models of K-Ras-driven lung and pancreatic tumors: validation of therapeutic targets. *Cold Spring Harb Perspect Med.* 2018;8(5).
36. Jaeger M G, and Winter G E. Fast-acting chemical tools to delineate causality in transcriptional control. *Mol Cell.* 2021;81(8):1617-1630.
37. Bilal F, et al. The transcription factor SLUG uncouples pancreatic cancer progression from the RAF-MEK1/2-ERK1/2 pathway. *Cancer Res.* 2021;81(14):3849-3861.
38. Abuhashem A, et al. Rapid and efficient degradation of endogenous proteins in vivo identifies stage-specific roles of RNA Pol II pausing in mammalian development. *Dev Cell.* 2022;57(8):1068-1080 e1066.
39. Yenerall P, et al. Use of the dTAG system in vivo to degrade CDK2 and CDK5 in adult mice and explore potential safety liabilities. *Toxicol Sci.* 2023;194(1):53-69.
40. Lin S, et al. An *in vivo* CRISPR screening platform for prioritizing therapeutic targets in AML. *Cancer Discov.* 2022;12(2):432-449.
41. Vichas A, et al. Integrative oncogene-dependency mapping identifies RIT1 vulnerabilities and synergies in lung cancer. *Nat Commun.* 2021;12(1):4789.
42. Lo A, et al. Multiomic characterization of oncogenic signaling mediated by wild-type and mutant RIT1. *Sci Signal.* 2021;14(711):eabc4520.
43. Akbay E A, et al. Interleukin-17A promotes lung tumor progression through neutrophil attraction to tumor sites and mediating resistance to PD-1 blockade. *J Thorac Oncol.* 2017;12(8):1268-1279.
44. Jackson E L, et al. Analysis of lung tumor initiation and progression using conditional expression of oncogenic K-ras. *Genes Dev.* 2001;15(24):3243-3248.
45. Briere D M, et al. The $KRAS^{G12C}$ inhibitor MRTX849 reconditions the tumor immune microenvironment and sensitizes tumors to checkpoint inhibitor therapy. *Mol Cancer Ther.* 2021;20(6):975-985.

46. Molina-Arcas M, and Downward J. Exploiting the therapeutic implications of KRAS inhibition on tumor immunity. *Cancer Cell.* 2024;42(3):338-357.
47. Pan Y, et al. Tumor-associated macrophages in tumor immunity. *Front Immunol.* 2020;11:583084.
48. Wang S, et al. Targeting M2-like tumor-associated macrophages is a potential therapeutic approach to overcome antitumor drug resistance. *NPJ Precis Oncol.* 2024;8(1):31.
49. Chen J, et al. Single-cell transcriptome and antigen-immunoglobin analysis reveals the diversity of B cells in non-small cell lung cancer. *Genome Biol.* 2020;21(1):152.
50. Zilionis R, et al. Single-cell transcriptomics of human and mouse lung cancers reveals conserved myeloid populations across individuals and species. *Immunity.* 2019;50(5):1317-1334 e1310.
51. Jablonski K A, et al. Novel markers to delineate murine M1 and M2 macrophages. *PLoS One.* 2015;10(12):e0145342.
52. Bod L, et al. B-cell-specific checkpoint molecules that regulate anti-tumour immunity. *Nature.* 2023;619(7969):348-356.
53. Morgan D, and Tergaonkar V. Unraveling B cell trajectories at single cell resolution. *Trends Immunol.* 2022;43(3):210-229.
54. Lambrechts D, et al. Phenotype molding of stromal cells in the lung tumor microenvironment. *Nat Med.* 2018;24(8):1277-1289.
55. Li H, et al. Fc Receptor-like 5 expression distinguishes two distinct subsets of human circulating tissue-like memory B cells. *J Immunol.* 2016;196(10):4064-4074.
56. Kim C C, et al. FCRL5^{+} memory B cells exhibit robust recall responses. *Cell Rep.* 2019;27(5):1446-1460 e1444.
57. Paiva S L, and Crews C M. Targeted protein degradation: elements of PROTAC design. *Curr Opin Chem Biol.* 2019;50:111-119.
58. Lee J K, et al. Comprehensive pan-cancer genomic landscape of KRAS altered cancers and real-world outcomes in solid tumors. *NPJ Precis Oncol.* 2022;6(1):91.
59. Fernandez Montes A, et al. The frequency of specific KRAS mutations, and their impact on treatment choice and survival, in patients with metastatic colorectal cancer. *Oncologist.* 2023;28(10):e902-e9.
60. Skoulidis F, et al. Sotorasib for lung cancers with *KRAS p.*G12C mutation. *N Engl J Med.* 2021;384(25):2371-2381.
61. Janne P A, et al. Adagrasib in non-small-cell lung cancer harboring a *KRAS*^{G12C} mutation. *N Engl J Med.* 2022;387(2):120-131.
62. Zhang Z, et al. A covalent inhibitor of K-Ras(G12C) induces MHC class I presentation of haptenated peptide neoepitopes targetable by immunotherapy. *Cancer Cell.* 2022;40(9):1060-1069 e1067.
63. Hattori T, et al. Creating MHC-restricted neoantigens with covalent inhibitors that can be targeted by immune therapy. *Cancer Discov.* 2023;13(1):132-145.
64. Nirala B K, et al. MYC regulates CSF-1 expression via microRNA 17/20a to modulate tumor-associated macrophages in osteosarcoma. *JCI Insight.* 2023.
65. Radko-Juettner S, et al. Targeting DCAF5 suppresses SMARCB1-mutant cancer by stabilizing SWI/SNF. *Nature.* 2024;628(8007):442-449.
66. Vetma V, et al. Confounding factors in targeted degradation of short-lived proteins. *ACS Chem Biol.* 2024;19(7):1484-1494.
67. Mehta S, et al. Temporal resolution of gene derepression and proteome changes upon PROTAC-mediated degradation of BCL11A protein in erythroid cells. *Cell Chem Biol.* 2022;29(8):1273-1287 e1278.
68. Yang F, et al. Efficient targeted oncogenic KRAS^{G12C} degradation via first reversible-covalent PROTAC. *Eur J Med Chem.* 2022;230:114088.

69. Kim D, et al. Pan-KRAS inhibitor disables oncogenic signalling and tumour growth. *Nature*. 2023;619(7968):160-166.
70. Holderfield M, et al. Concurrent inhibition of oncogenic and wild-type RAS-GTP for cancer therapy. *Nature*. 2024;629(8013):919-926.
71. Wasko U N, et al. Tumour-selective activity of RAS-GTP inhibition in pancreatic cancer. *Nature*. 2024;629(8013):927-936.
72. Schulze C J, et al. Chemical remodeling of a cellular chaperone to target the active state of mutant KRAS. *Science*. 2023;381(6659):794-799.
73. Sulahian R, et al. Synthetic lethal interaction of SHOC2 depletion with MEK inhibition in RAS-driven cancers. *Cell Rep*. 2019;29(1):118-134 e118.

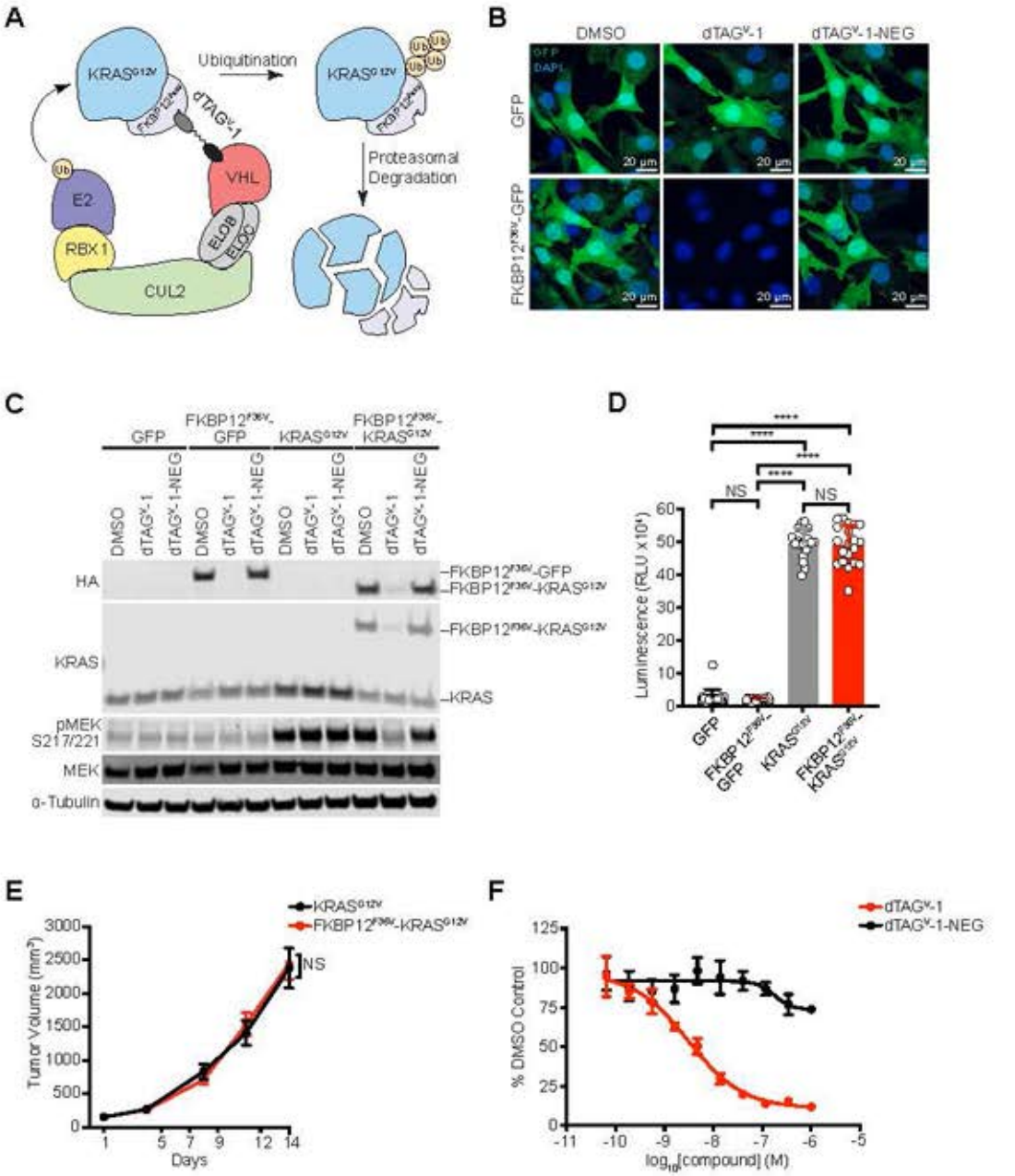

Figure 1. Validation of targeted degradation of KRAS^{G12V} using the dTAG system. (**A**) Schematic of the dTAG system showing that dTAG^{V}-1 recruits the von Hippel-Lindau (VHL) E3 ubiquitin ligase to induce targeted degradation of FKBP12^{F36V}-KRAS^{G12V}. (**B**) Representative images of NIH/3T3 cells expressing GFP or FKBP12^{F36V}-GFP treated with DMSO, 500 nM dTAG^{V}-1, or 500 nM dTAG^{V}-1-NEG for 8 h. The scale bar represents 20 μm. Data is representative of *n* = 3 independent experiments. (**C**) Immunoblot analysis of HA to detect FKBP12^{F36V}-GFP or FKBP12^{F36V}-KRAS^{G12V}, KRAS, pMEK, MEK, and α-Tubulin of NIH/3T3 cells expressing GFP, FKBP12^{F36V}-GFP, KRAS^{G12V}, or FKBP12^{F36V}-KRAS^{G12V} treated with DMSO, 500 nM dTAG^{V}-1, or 500 nM dTAG^{V}-1-NEG for 8 h. Data is representative of *n* = 3 independent experiments. (**D**) Antiproliferation of NIH/3T3 cells expressing GFP, FKBP12^{F36V}-GFP, KRAS^{G12V}, or FKBP12^{F36V}-KRAS^{G12V} cultured as ultra-low adherent 3D-spheroid suspensions for 144 h. Data is presented as mean ± s.d. of *n* = 20 biologically independent samples and are representative of *n* = 3 independent experiments. RLU = Relative light units. (**E**) Tumor volume changes of NIH/3T3 cells expressing KRAS^{G12V} or FKBP12^{F36V}-KRAS^{G12V} that were subcutaneously injected into mice. Data is presented as mean ± SEM from *n* = 10 per group. (**F**) DMSO-normalized proliferation of NIH/3T3 cells expressing FKBP12^{F36V}-KRAS^{G12V} cultured as ultra-low adherent 3D-spheroid suspensions and treated with the indicated compounds for 120 h. Data is presented as mean ± s.d. of *n* = 4 biologically independent samples and are representative of *n* = 3 independent experiments. ****P < 0.0001 (**D**) and non-significant (NS) (**D-E**) by a one-way ANOVA with post hoc Tukey's test (**D**) or a two-tailed Student's *t*-test (**E**).

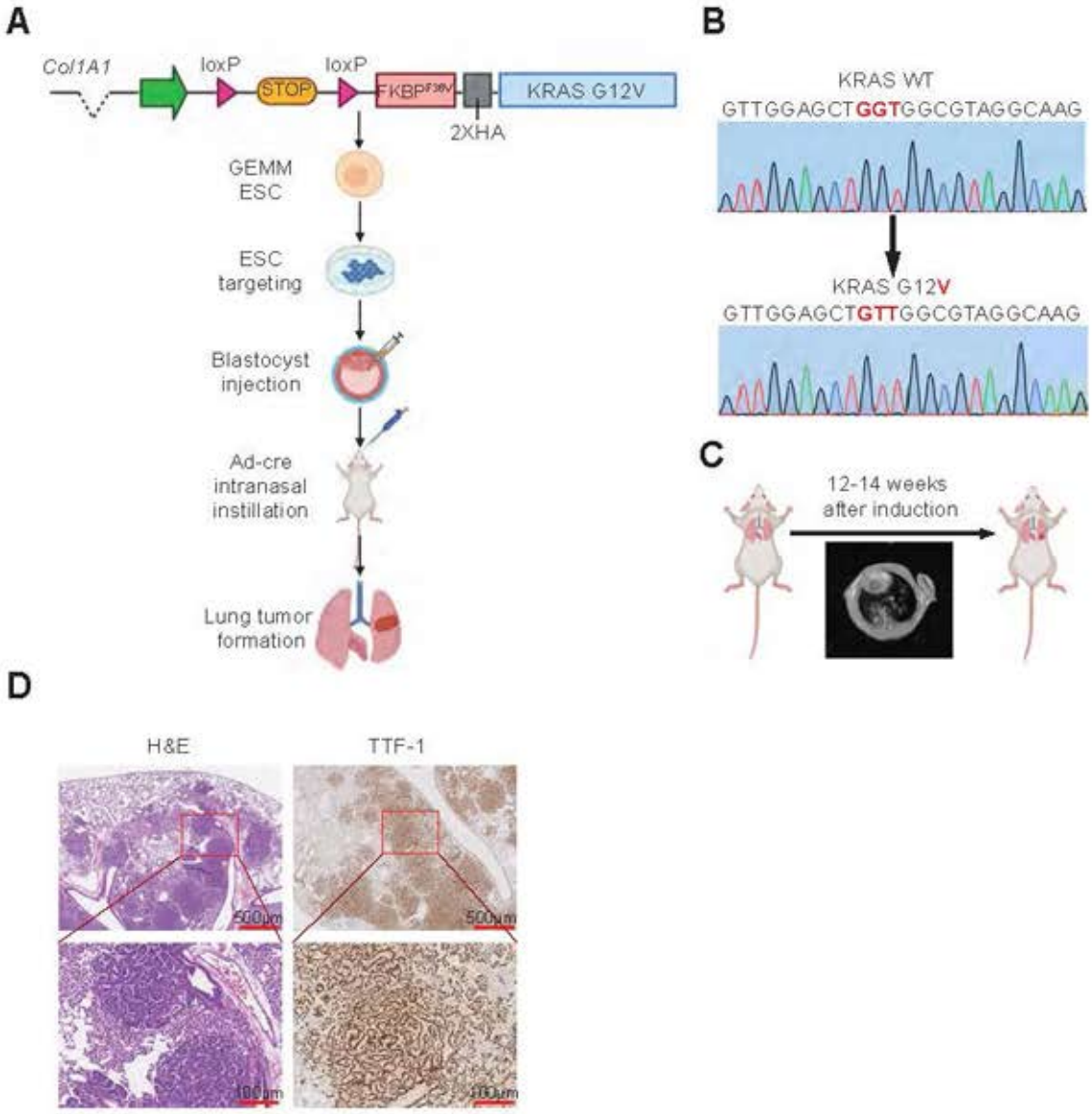

Figure 2. Establishing a GEMM for targeted degradation of KRAS^{G12V} in lung cancer. (**A**) Schematic showing the design of the *FKBP12^{F36V}-KRAS^{G12V}* GEMM. (**B**) Genomic sequencing confirmation of *KRAS^{G12V}* mutation in the GEMM. (**C**) MRI was performed to detect lung tumor nodules 12-14 weeks after adenovirus-carrying Cre recombinase delivery. (**D**) Representative images of hematoxylin and eosin (H&E) and immunohistochemistry (IHC) for TTF-1 of lung tumors from the *FKBP12^{F36V}-KRAS^{G12V}* GEMM. The scale bar represents 500 and 100 μm from top to bottom.

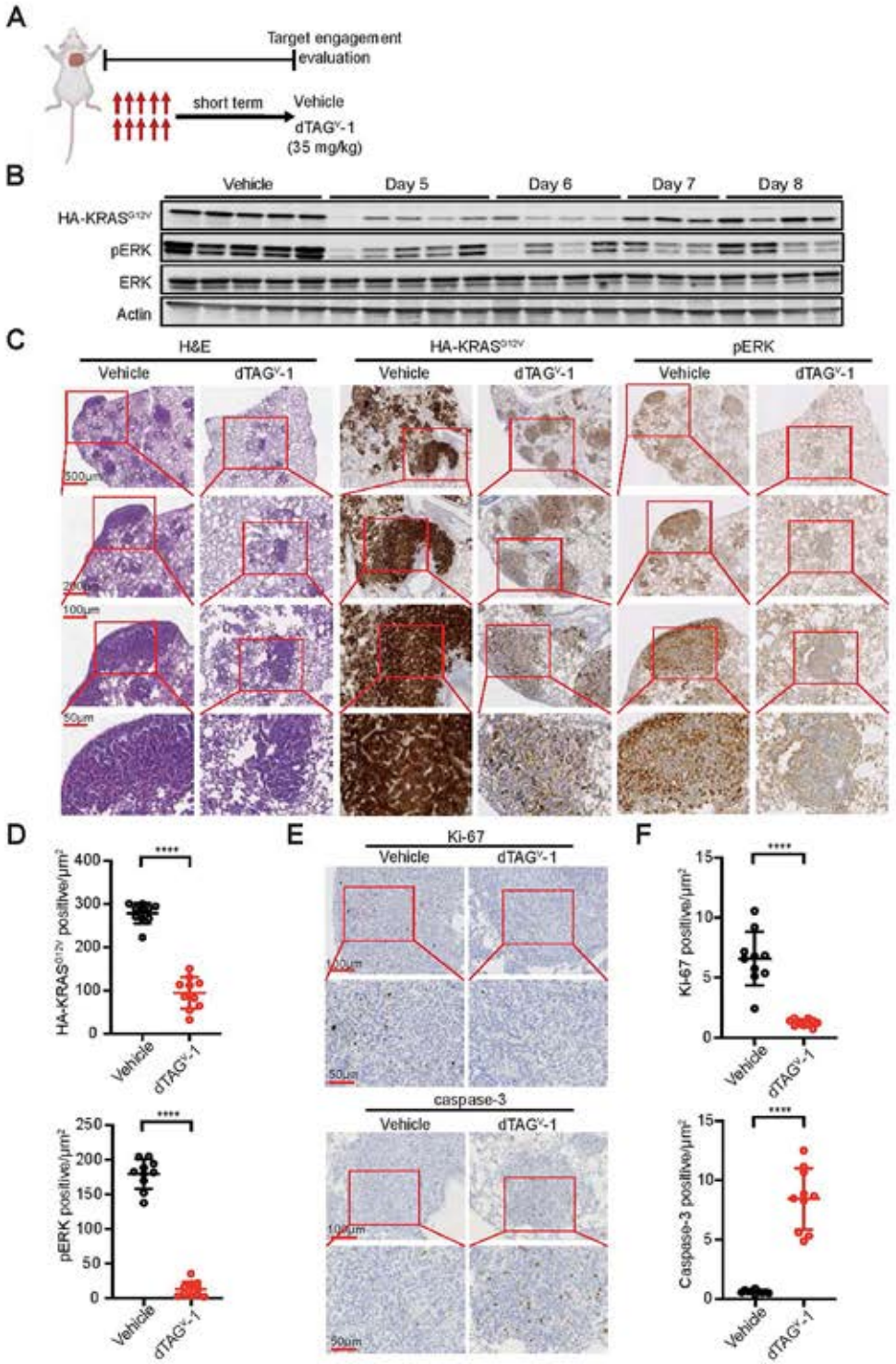

Figure 3. dTAG^V-1 effectively degrades KRAS^{G12V} and inhibits downstream signaling in a *KRAS^{G12}*-driven lung cancer GEMM. (**A**) Schematic showing the *in vivo* dosing schedule for evaluating target engagement and degradation. Mice were treated once daily with either vehicle or dTAG^V-1 (35 mg/kg) for 5 days. (**B**) Immunoblot analysis of HA to detect FKBP12^{F36V}-KRAS^{G12V}, pERK, ERK, and actin in lung tumor nodules after the indicated treatment and time from *n* = 3-5 per group. (**C**) Representative images of H&E and IHC staining for HA to detect FKBP12^{F36V}-KRAS^{G12V} and pERK of lung tumors after the indicated treatment from *n* = 3 per group. The scale bar represents 500, 200, 100 and 50 μm from top to bottom. (**D**) Quantification of HA to detect FKBP12^{F36V}-KRAS^{G12V} and pERK positive staining after the indicated treatment. Data is presented as mean ± s.d. of ten representative areas from *n* = 3 mice per group. (**E**) Representative images of IHC staining for Ki-67 and cleaved caspase-3 of lung tumors after the indicated treatment. The scale bar represents 100 and 50 μm for top and bottom. (**F**) Quantification of Ki-67 and cleaved caspase-3 positive staining after the indicated treatment. Data is presented as mean ± s.d. of ten representative areas from *n* = 3 mice per group. ****$P < 0.0001$ (**D** and **F**) by a two-tailed Student's *t*-test.

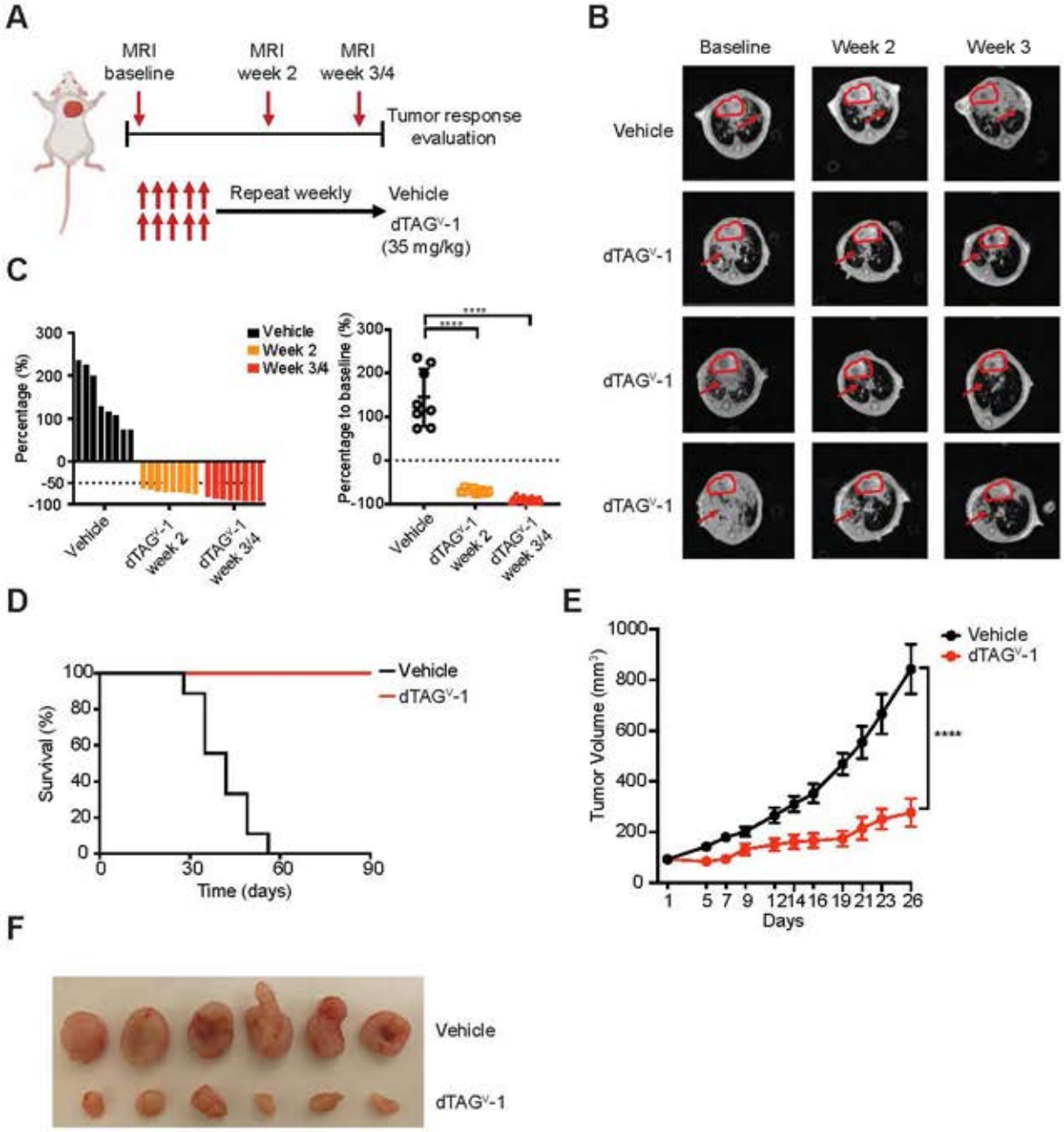

Figure 4. KRAS^{G12V} degradation abolishes tumor growth in *KRAS^{G12V}*-driven murine lung and pancreatic cancer models. (**A**) Schematic showing the *in vivo* dosing schedule for evaluating long-term dTAG^{V}-1 treatment. (**B**) Representative MRI scans (one vehicle and three dTAG^{V}-1 treated mice) of tumor baseline, 2 weeks, and 3 weeks after treatment initiation. The red arrowheads indicate lung tumors, and the red circles indicate the heart. (**C**) Waterfall plot and dot plot showing changes in tumor volume compared to baseline after 2 or 3/4 weeks of treatment. Data is presented as mean ± s.d. from n = 8 per group. (**D**) Kaplan-Meier survival curve of *FKBP12^{F36V}-KRAS^{G12V}* lung cancer mice after long-term treatment with vehicle or dTAG^{V}-1 from n = 9 per group. (**E**) Tumor volume changes of PATU-8902 FKBP12^{F36V}-KRAS^{G12V}; *KRAS$^{-/-}$* cells that were subcutaneously injected into mice and treated with vehicle or dTAG^{V}-1. Data is presented as mean ± SEM from n = 12 per group. (**F**) Representative pancreatic tumors after the indicated treatment. ****P < 0.0001 by a one-way ANOVA with post hoc Dunnett's test (**C**) and a two-tailed Student's t-test (**E**).

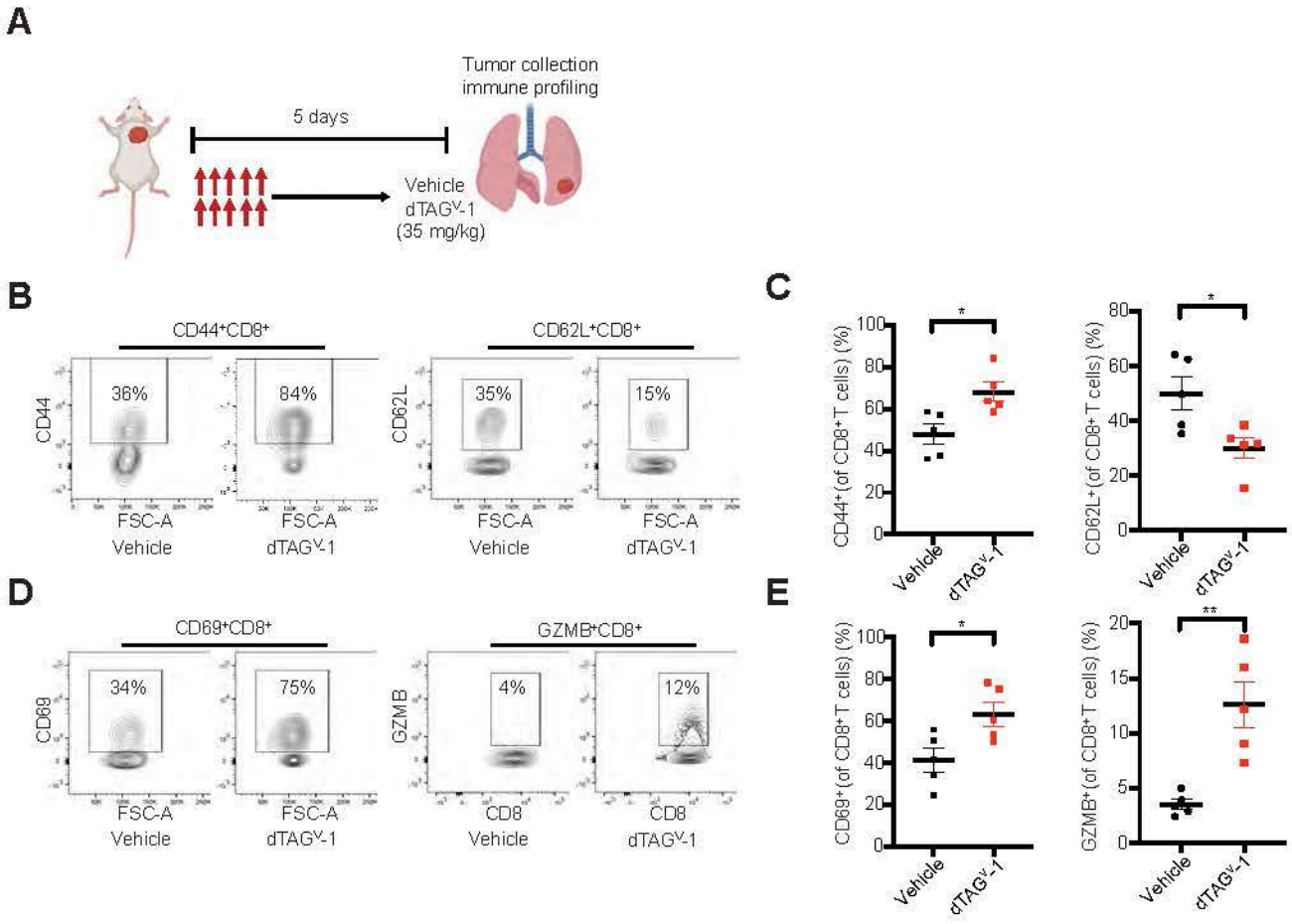

Figure 5. KRAS^{G12V} degradation increases CD8$^+$ T activity in a *KRAS^{G12V}*-driven lung cancer GEMM. (**A**) Schematic showing the experimental design for immune profiling. After confirming tumor burden by MRI, mice were randomized and treated once daily with either vehicle or dTAG^V-1 (35 mg/kg) for 5 days. Tumor nodules were then collected, and tumor-infiltrating lymphocytes were analyzed by flow cytometry. (**B** and **C**) Frequencies of CD44$^+$ CD8$^+$ T cells and CD62L$^+$ CD8$^+$ T cells from $n = 5$ per group. Data is presented as mean ± SEM (**C**). (**D** and **E**) Frequencies of CD69$^+$ CD8$^+$ T cells and GZMB$^+$ CD8$^+$ T cells from $n = 5$ per group. Data is presented as mean ± SEM (**E**). *$P < 0.05$ and **$P < 0.01$ (**C** and **E**) by a two-tailed Student's *t*-test.

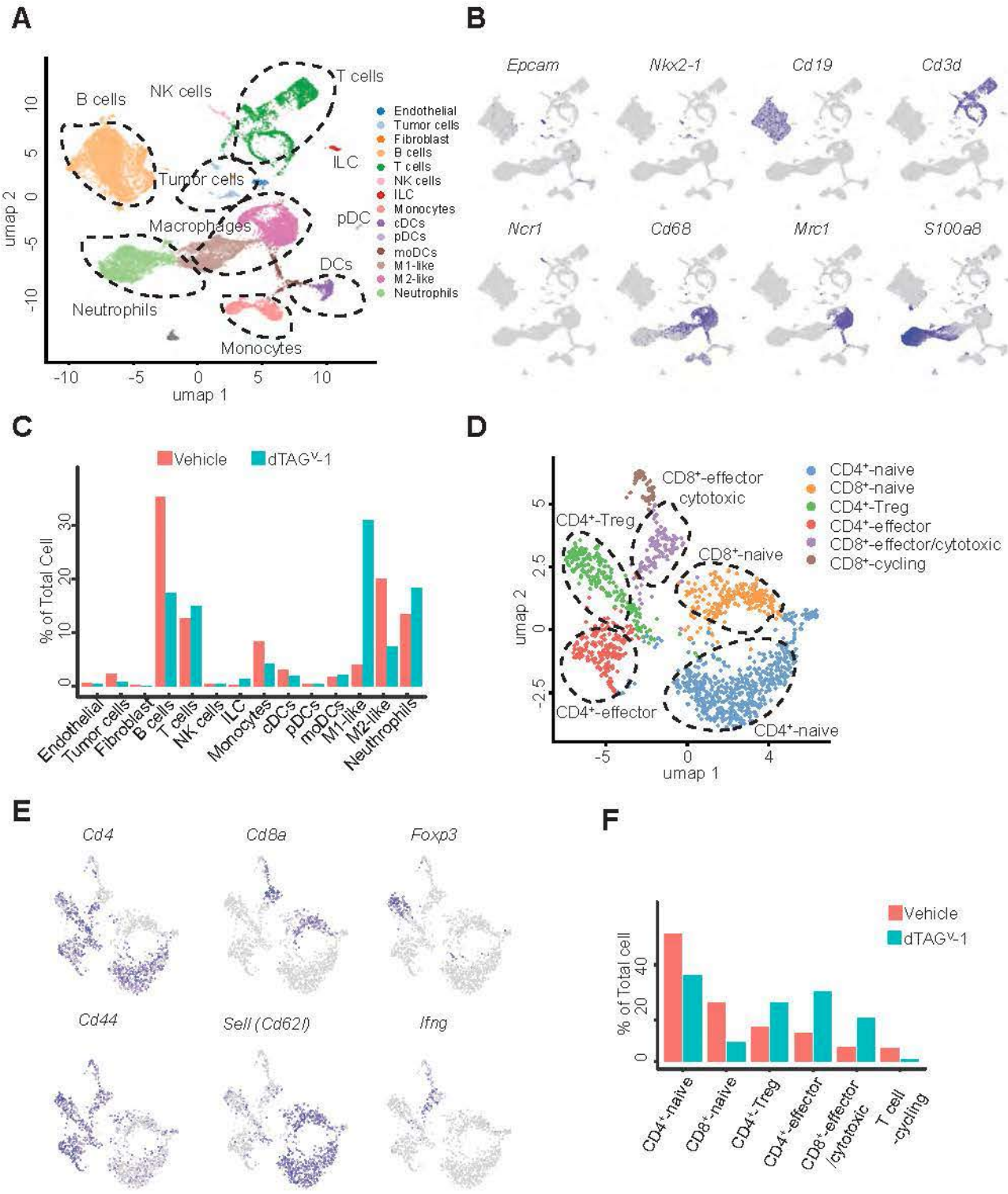

Figure 6. Single-cell RNA-seq reveals KRAS^{G12V} degradation reprograms the TME to promote antitumor immunity in a *KRAS^{G12V}*-driven lung cancer GEMM. (**A**) UMAP plot showing identified cell populations including tumor cells, immune cells, and fibroblasts. (**B**) UMAP plots showing the expression of cell-type specific marker genes. (**C**) Percentage of cells in TME of annotated clusters in response to the indicated treatments. (**D**) UMAP plot showing identified cell subsets in T cell population. (**E**) UMAP plots show the expression of selected marker genes. (**F**) Percentage of cells in the annotated T cell subsets in response to the indicated treatments.

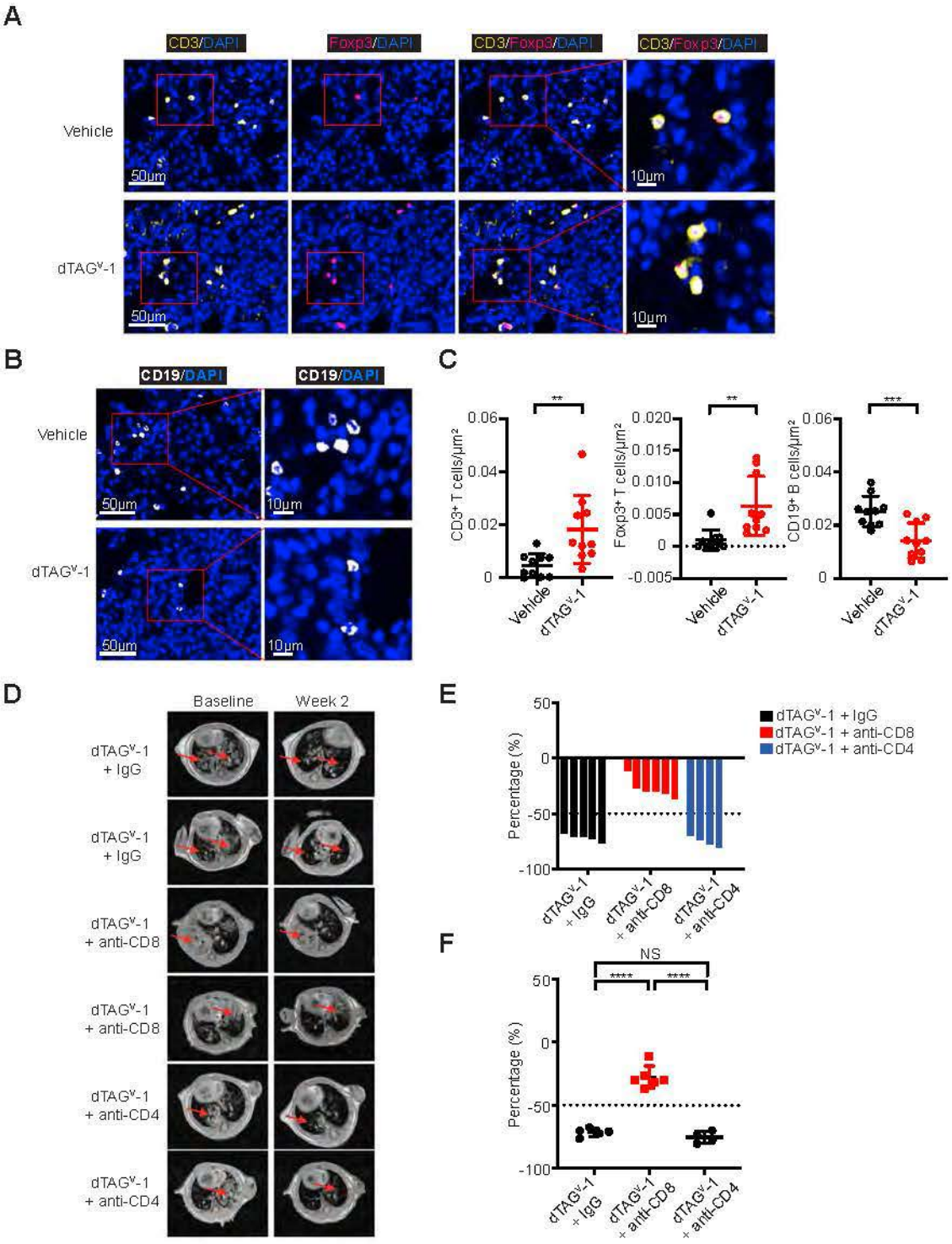

Figure 7. Antitumor immunity by KRAS^{G12V} degradation is partly dependent on CD8$^+$ T cells in a *KRAS^{G12V}*-driven lung cancer GEMM. (**A** and **B**) Representative multiplex IF images showing (**A**) tumor infiltrating CD3$^+$ T cells, Foxp3$^+$ Treg cells and (**B**) CD19$^+$ B cells in response to indicated treatment. The same samples are presented in **A** and **B**. The scale bar represents 50 and 10 μm from left to right, respectively. (**C**) Quantification of CD3$^+$ T cells, Foxp3$^+$ Treg cells and CD19$^+$ B cells in response to the indicated treatment. Data is presented as mean ± s.d. of ten representative areas from n = 3 mice per group. (**D**) Representative MRI scans of lung tumors at baseline and 2 weeks in response to indicated treatment. The red arrowheads indicate lung tumors. (**E** and **F**) Waterfall plot (**E**) and dot plot (**F**) showing changes in tumor volume compared to baseline after 2 weeks of treatment. Data is presented as mean ± s.d. from n = 4-6 per group. $^{**}P < 0.01$, $^{***}P < 0.001$, $^{****}P < 0.0001$ and non-significant (NS) by a two-tailed Student's t-test (**C**) and a one-way ANOVA with post hoc Tukey's test (**F**).